

REPORT DOCUMENTATION PAGE

Form Approved OMB NO. 0704-0188

The public reporting burden for this collection of information is estimated to average 1 hour per response, including the time for reviewing instructions, searching existing data sources, gathering and maintaining the data needed, and completing and reviewing the collection of information. Send comments regarding this burden estimate or any other aspect of this collection of information, including suggestions for reducing this burden, to Washington Headquarters Services, Directorate for Information Operations and Reports, 1215 Jefferson Davis Highway, Suite 1204, Arlington VA 22202-4302. Respondents should be aware that notwithstanding any other provision of law, no person shall be subject to any penalty for failing to comply with a collection of information if it does not display a currently valid OMB control number.
PLEASE DO NOT RETURN YOUR FORM TO THE ABOVE ADDRESS.

1. REPORT DATE (DD-MM-YYYY) 13-02-2015	2. REPORT TYPE Final Report	3. DATES COVERED (From - To) 5-Dec-2011 - 4-Dec-2014		
4. TITLE AND SUBTITLE Final Report: Mitigating Stress Waves by Using Nanofoams and Nanohoneycombs		5a. CONTRACT NUMBER W911NF-12-1-0011		
		5b. GRANT NUMBER		
		5c. PROGRAM ELEMENT NUMBER 611102		
6. AUTHORS Yu Qiao		5d. PROJECT NUMBER		
		5e. TASK NUMBER		
		5f. WORK UNIT NUMBER		
7. PERFORMING ORGANIZATION NAMES AND ADDRESSES University of California - San Diego 9500 Gilman Drive MC 0934 La Jolla, CA 92093 -0934		8. PERFORMING ORGANIZATION REPORT NUMBER		
9. SPONSORING/MONITORING AGENCY NAME(S) AND ADDRESS (ES) U.S. Army Research Office P.O. Box 12211 Research Triangle Park, NC 27709-2211		10. SPONSOR/MONITOR'S ACRONYM(S) ARO		
		11. SPONSOR/MONITOR'S REPORT NUMBER(S) 58458-MS.3		
12. DISTRIBUTION AVAILABILITY STATEMENT Approved for Public Release; Distribution Unlimited				
13. SUPPLEMENTARY NOTES The views, opinions and/or findings contained in this report are those of the author(s) and should not be construed as an official Department of the Army position, policy or decision, unless so designated by other documentation.				
14. ABSTRACT In this ARO project, we had a remarkable finding: In dynamic indentation test, the indentation size of a silica nanofoam was smaller than in a solid silica; i.e. the former was effectively "harder" than the latter. All the samples were in the same amorphous silica phase; the porosity of all nanofoam samples was ~60%, and therefore, their mass density was only ~40% of that of solid silica. The experiment was conducted in a Split Hopkinson Bar (SHB) setup. A titanium striker impacted on a steel incident bar at ~8.5 m/s; the incident bar forced a hard hemispherical indenter into the silica sample. The silica sample was sandwiched in between the indenter and a steel transmitted bar.				
15. SUBJECT TERMS Nanofoam; Protection; Stress Wave; Damping; Energy absorption; Dynamic behavior				
16. SECURITY CLASSIFICATION OF: a. REPORT UU		17. LIMITATION OF ABSTRACT UU	15. NUMBER OF PAGES	19a. NAME OF RESPONSIBLE PERSON Yu Qiao
b. ABSTRACT UU				19b. TELEPHONE NUMBER 858-534-3388
Standard Form 298 (Rev 8/98) Prescribed by ANSI Std. Z39.18				

Report Title

Final Report: Mitigating Stress Waves by Using Nanofoams and Nanohoneycombs

ABSTRACT

In this ARO project, we had a remarkable finding: In dynamic indentation test, the indentation size of a silica nanofoam was smaller than in a solid silica; i.e. the former was effectively “harder” than the latter. All the samples were in the same amorphous silica phase; the porosity of all nanofoam samples was ~60%, and therefore, their mass density was only ~40% of that of solid silica. The experiment was conducted in a Split Hopkinson Bar (SHB) setup. A titanium striker impacted on a steel incident bar at ~8.5 m/s; the incident bar forced a hard hemispherical indenter into the silica sample. The silica sample was sandwiched in between the indenter and a steel transmitted bar.

This counter-intuitive phenomenon was observed only in dynamic tests. Quasi-static indentation results fitted with the classic theory quite well.

The silica nanofoam also had an excellent energy absorption performance under dynamic shear loadings. In a SHB system, silica nanofoam disk sample was sandwiched in between the incident bar and a shear-promotion ring (SPR). The portion of the material in the circular band between the outer surface of incident bar and the inner surface of SPR was subjected to dynamic shear. The transmitted wave pressure significantly decreased with the pore size; i.e. a silica nanofoam was “softer” than a larger-pore-sized foam. In all the tests, the incident stress waves were similar.

This pore size effect was observed only when the stress wave was highly heterogeneous. Under a quasi-static shear loading or an uniform dynamic compression loading, the sample behaviors were quite independent of the pore size, as predicted by classic theory.

The excellent dynamic performance of silica nanofoams was attributed to the local hardening effect of nanopore collapse: As the nanopore size is much smaller than the characteristic length of indenter or stress wave front, nanopore buckling can be sufficiently fast and be viewed as a local condensation process. Thus, shear localization associated with local softening in a regular foam is suppressed, and bulk energy absorption is achieved.

Enter List of papers submitted or published that acknowledge ARO support from the start of the project to the date of this printing. List the papers, including journal references, in the following categories:

(a) Papers published in peer-reviewed journals (N/A for none)

Received Paper

TOTAL:

Number of Papers published in peer-reviewed journals:

(b) Papers published in non-peer-reviewed journals (N/A for none)

Received Paper

TOTAL:

Number of Papers published in non peer-reviewed journals:

(c) Presentations

Number of Presentations: 0.00

Non Peer-Reviewed Conference Proceeding publications (other than abstracts):

Received Paper

TOTAL:

Number of Non Peer-Reviewed Conference Proceeding publications (other than abstracts):

Peer-Reviewed Conference Proceeding publications (other than abstracts):

Received Paper

TOTAL:

Number of Peer-Reviewed Conference Proceeding publications (other than abstracts):

(d) Manuscripts

Received Paper

TOTAL:

Number of Manuscripts:

Books

Received Book

TOTAL:

Received Book Chapter

TOTAL:

Patents Submitted

Patents Awarded

Awards

Graduate Students

<u>NAME</u>	<u>PERCENT SUPPORTED</u>	Discipline
Weiyi Lu	0.50	
Cang Zhao	1.00	
FTE Equivalent:	1.50	
Total Number:	2	

Names of Post Doctorates

<u>NAME</u>	<u>PERCENT SUPPORTED</u>
Weiyi Lu	0.50
FTE Equivalent:	0.50
Total Number:	1

Names of Faculty Supported

<u>NAME</u>	<u>PERCENT_SUPPORTED</u>	National Academy Member
Yu Qiao	0.20	No
FTE Equivalent:	0.20	
Total Number:	1	

Names of Under Graduate students supported

<u>NAME</u>	<u>PERCENT_SUPPORTED</u>
FTE Equivalent:	
Total Number:	

Student Metrics

This section only applies to graduating undergraduates supported by this agreement in this reporting period

The number of undergraduates funded by this agreement who graduated during this period: 0.00

The number of undergraduates funded by this agreement who graduated during this period with a degree in science, mathematics, engineering, or technology fields:..... 0.00

The number of undergraduates funded by your agreement who graduated during this period and will continue to pursue a graduate or Ph.D. degree in science, mathematics, engineering, or technology fields:..... 0.00

Number of graduating undergraduates who achieved a 3.5 GPA to 4.0 (4.0 max scale):..... 0.00

Number of graduating undergraduates funded by a DoD funded Center of Excellence grant for Education, Research and Engineering:..... 0.00

The number of undergraduates funded by your agreement who graduated during this period and intend to work for the Department of Defense 0.00

The number of undergraduates funded by your agreement who graduated during this period and will receive scholarships or fellowships for further studies in science, mathematics, engineering or technology fields:..... 0.00

Names of Personnel receiving masters degrees

<u>NAME</u>
Total Number:

Names of personnel receiving PHDs

<u>NAME</u>	
Weiyi Lu	
Cang Zhao	
Total Number:	2

Names of other research staff

<u>NAME</u>	<u>PERCENT_SUPPORTED</u>
FTE Equivalent:	
Total Number:	

Sub Contractors (DD882)

Inventions (DD882)

5 Nanofoams for protection and damping

Patent Filed in US? (5d-1) N

Patent Filed in Foreign Countries? (5d-2) N

Was the assignment forwarded to the contracting officer? (5e) N

Foreign Countries of application (5g-2):

5a: Cang Zhao

5f-1a: UCSD

5f-c: 9500 Gilman Dr. MC 0085

CA 92093

5a: Yu Qiao

5f-1a: UCSD

5f-c: 9500 Gilman Dr. MC 0085

CA 92093

Scientific Progress

Please see the attachment

Technology Transfer

FINAL REPORT

Date: February 12th, 2015

Period of Performance: December 5th, 2011 – December 4th, 2014

Project Title: Mitigating Stress Waves Using Nanofoams and Nanohoneycombs

Grant No.: W911NF-12-1-0011

Program Manager: Dr. David M. Stepp

PI: Professor Yu Qiao

Department of Structural Engineering

University of California – San Diego

9500 Gilman Dr. MC 0085, La Jolla, CA 92093-0085

Phone: 858-534-3388

Email: yqiao@ucsd.edu

Other Personnel Involved in the Project:

Dr. Weiyi Lu, Postdoctoral Researcher

Mr. Cang Zhao, Graduate Student Researcher

TABLE OF ONTENTS

Table of ontents	1
SUMMARY OF ACHEIVEMENTS.....	3
1. Background and Hypothesis	4
2. Processing of Silica Nanofoams	7
2.1 Preparation of Silica Monoliths.....	7
2.2 High-Temperature Post-Processing Treatment of Silica Monoliths	8
2.3 Polishing of Silica Foams.....	10
2.4 Characterization of Silica Foams	11
2.4.1 Porosity	11
2.4.2 Pore Size	11
2.4.3 Phase	14
2.4.4 Morphology.....	14
3. Development of Testing systems.....	15
3.1 Development of Split Hopkinson Bar System	15
3.2 Development of Shear Promotion Holder.....	16
3.3 Quasi-static Shear Tests	17
3.4 Dynamic Compression Tests.....	19
3.5 Dynamic Shear Tests.....	19
4. Quantitative SEM Image Analysis	20
4.1 Two Dimensional Nominal Porosity.....	20
4.2 Harvesting SEM Samples.....	21
4.2.1 Low impact velocity tests	21
4.2.2 High impact velocity tests.....	22
4.3 Strategy of SEM Scanning	22
4.4 Image Analysis.....	31
5. Two-parameter Study on Silica Foams.....	32
5.1 Two-parameter Silica Foams	32
5.2 Quasi-static Shear Tests	34
5.3 Dynamic Shear Tests.....	34
5.4 Deformation Zone	37
6. Single-parameter Study on Silica Foams.....	42

6.1	Single-parameter Silica Foams.....	42
6.2	Quasi-static Shear Tests	43
6.3	Dynamic Compression Tests.....	44
6.4	Dynamic Shear Tests.....	44
6.4.1	Transmitted wave pressure	44
6.4.2	Pressure Reduction.....	44
6.4.3	Energy Absorption	45
6.5	Deformation Zone	47
7.	Analysis of Effects of Shear Strain Rate.....	48
7.1	Pore Size Effect.....	49
7.2	Effects of Impact Rate.....	51
7.2.1	Transmitted Wave Pressure	52
7.2.2	Transmitted Wave Energy	53
7.2.3	Energy Absorption	54
7.3	Effects of Shear Gap Width	56
7.3.1	Transmitted Wave Pressure	56
7.3.2	Transmitted Wave Energy	57
8.	Dynamic Indentation Tests	60
8.1	Single-parameter Silica Foams.....	60
8.2	Indentation Tests	61
8.3	Testing Results	63
9.	Conclusions and Future Work.....	66
APPENDIX.....		67
A. Mechanical Drawings of Shear Promotion Holder		67
B. Codes for SEM Image Enhancement		69
C. Dynamic indentation.....		71
REFERENCES.....		73

SUMMARY OF ACHEIVEMENTS

Our major experimental results are presented in Section 6 and Section 8 below.

In the past three years, we conducted quasi-static tests and SHB dynamic tests on silica foam samples, and performed comprehensive data and image analysis. The results demonstrated a consistent, strong correlation between the pore size and the dynamic behaviors of the silica foams: Reducing the pore size to below ~200 nm has a significant beneficial effect on suppressing shear band formation and promoting widespread energy absorption.

This size effect is attributed to the ultra-fast local hardening associated with the condensation of nanopores, compared to relatively slow local softening caused by collapse of larger pores. That is, without changing the network material and the porosity, decreasing the pore size of a foam to the nanometer scale (much smaller than the characteristic length of shear bands) would considerably help mitigate shear localization and enhance dynamic energy absorption.

Our experiential work began with the processing and treatment of silica nanofoam samples (Section 2), and the development of a forced-shear dynamic testing system (Section 3) and a quantitative SEM image analysis technique (Section 4). We then performed systematic experimental investigation on two-parameter nanofoam samples (Section 5), and eventually, on single-parameter samples (Section 6). The single-parameter samples are improved from two-parameter ones; the data of the former are much more conclusive, as shown in Section 7. In addition, we also conducted dynamic indentation experiments on silica foams (Section 8), and the results are consistent with the dynamic shearing data: The indentation radius and the penetration depth were largely reduced as the pore size of silica foam was decreased to the nanometer scale, with the porosity maintained nearly constant. The details of our work are presented below.

1. BACKGROUND AND HYPOTHESIS

Materials responses to dynamic loadings are often fundamentally different from their quasi-static behaviors. As the loading rate is sufficiently high, the loading mode is no longer equilibrium; rather, it would be governed by propagation, dispersion, reflection, and transmission of stress waves. While linear stress waves have been relatively well understood, intense, highly nonlinear stress waves are still relatively under-investigated. As the wave amplitude increases, its propagation may be coupled with the change in local material properties and structures. For instance, in a foam, as the wave pressure exceeds the buckling threshold of the cells, the cells would collapse as the wave front advances across them, and the loading and unloading processes are irreversible. Under this condition, linear wave theory breaks down and many unique phenomena would be observed, among which is wave localization [1] – As an initially uniform, intense stress wave propagates in a homogeneous material, its front may become unstable, and the wave energy tends to focus in a few narrow zones, known as shear bands [2].

The origin of the instability of an intense stress wave is related to its nonlinearity: Under the high, dynamic wave pressure, the local material undergoes a certain structural changes, e.g. cell buckling in a foam or microcracking in a solid metal/alloy [3], which causes permanent variation in local material properties. If the deformed zones are “softer” than the original material, wave energy tends to concentrate in such areas, resulting in increasingly pronounced variations in adjacent fields. As this process continues, the degree of heterogeneity and localization of stress wave rises, eventually leading to the formation of shear bands.

Wave localization can be harmful in a large number of cases. For instance, in a protection foam, if stress waves are focused in a few shear bands, the material can fail rapidly as the shear-banding occurs, with the majority of the material unchanged. The energy absorption capacity of the material outside the shear bands is essentially wasted, which is a main reason why the dynamic performance of a protection or damping material can be much lower than its quasi-static measurement results [4].

Note that nonlinearity does not necessarily always result in heterogeneity. If under the loading of an intense stress wave, the material undergoes local hardening instead of local softening, the internal damaging process may be helpful to maintain a stable wave front [5], as the wave energy tends to disperse to the undamaged, relatively “soft” area. For example, in a foam, usually when the cells buckle, the local area is softened. But if the pore size is much smaller than the width of shear band, cell collapse may be regarded as a local condensation mechanism, promoting the widespread of wave energy in a broader field. A smaller characteristic size also reduces the

characteristic response time, so that the material may react sufficiently fast to the sharp wave front, where the local pressure can rise to the peak value in a few microseconds (μs).

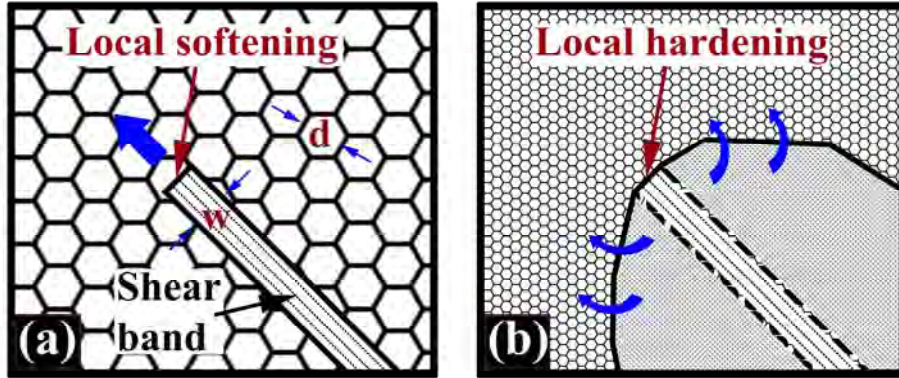


Fig. 1.1 Schematic of shear banding in foams (a) of a relatively large pore size and (b) of a relatively small pore size, compared with the shear band width.

Fig. 1.1 depicts shear banding in foams of different pore sizes. In Fig. 1.1 (a), the pore size, d , is comparable with or larger than the shear band width, w . As an intensive wave front arrives, the local cells are crushed, as the wave pressure, P_w , is higher than the buckling pressure, P_{cr} . The buckled cells form local “weak links” along the wave front, since usually the initiation of buckling demands a higher pressure than the continuation of buckling [6]. Consequently, it is energetically favorable for the wave energy to focus on the buckled cells and their surrounding areas, protruding forward and leaving the unbuckled cells behind. Eventually, the wave front propagation becomes unstable and shear bands are developed.

In Fig. 1.1 (b), the pore size is much smaller than the shear band width. Thus, the buckling of cells happens much faster than the characteristic time of wave front propagation. Before the wave energy can concentrate in narrow bands, the buckled cells have been condensed, resulting in a local hardening effect; that is, it demands a higher pressure to further compact a fully buckled cell than a hollow cell, as the buckling pressure, P_{cr} , is always lower than the yield strength of solid material, Y [6]. As the compaction at the stress wave front increases the effective strength of the buckled zones, the wave energy would widely spread to undamaged areas, so that the wave front becomes more stable.

The shear band width, w , is a function of the wave pressure (P_w), the pulse duration (t), the speed of sound (c), the pore size (d), the porosity (p), and the material strength (Y). Note that the critical

stress of cell buckling, P_{cr} , is related to pY [6], and thus, may not be regarded as an independent variable. That is,

$$w = f(P_w, t, c, d, Y, p) \quad (1)$$

where f is an unknown function. According to the Π Theorem [7], Eq.(1) can be rewritten as

$$w/d = f^*(P_w/Y, tc/d) \quad (2)$$

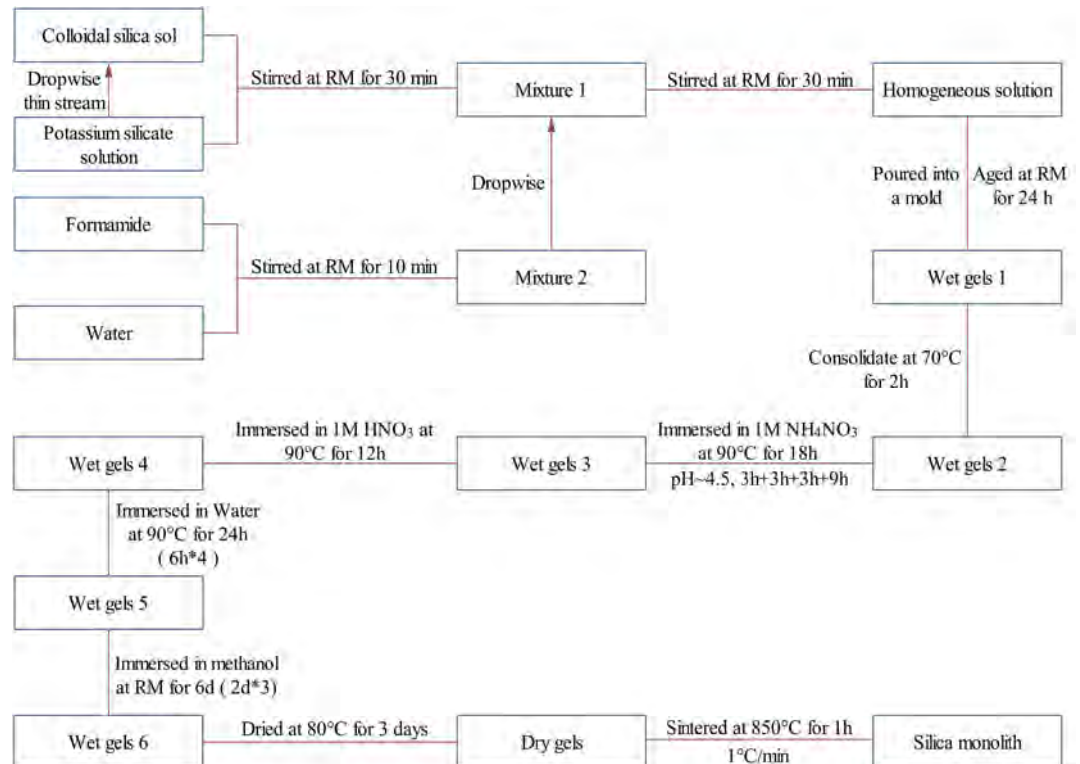
where f^* is an unknown function containing a dimensionless parameter, p . It can be seen that the ratio of the shear-band width to the pore size, w/d , is dependent on the pore size itself, due to the second term at the right-hand side (RHS) of Eq.(2), tc/d . That is, the shear-band width is not proportional to the pore size; as the pore size varies, their ratio, w/d , would change. Such a nonlinear relationship ensures that shear banding is not scalable to the pore size, making it feasible that the self-condensation mechanism discussed above may be activated by optimizing the pore size in a foam.

In order to promote local hardening associated with the collapse of cells much smaller than the shear band width, the ratio of w/d should be as large as possible. Because the forms of f and f^* are unknown, it is not clear whether the w/d ratio is positively or negatively correlated with the pore size, d . As a large number of experimental observations suggested that shear banding occurs in large-pore-sized foams, it is highly possible that the w/d ratio increases as the pore size, d , decreases; i.e. a small pore size, probably at the nm scale, would help enhance the local hardening effects of cell buckling, which in turn suppresses shear banding. The objective of the current research project is to test whether this hypothesis is against experimental data.

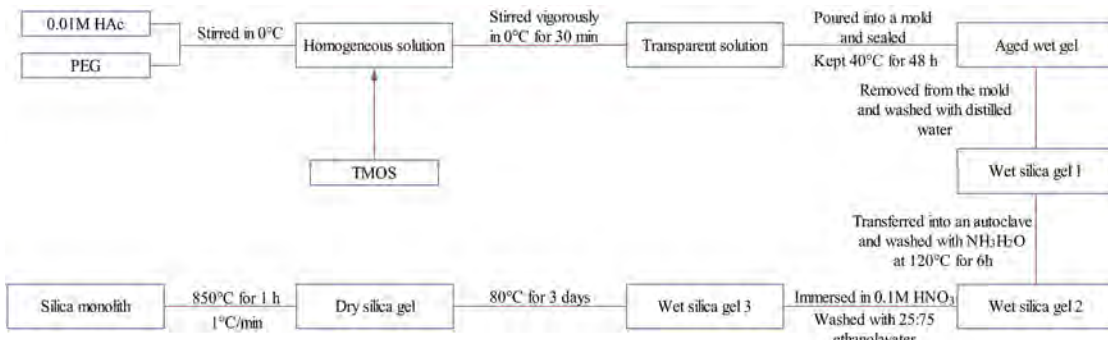
2. PROCESSING OF SILICA NANOFOAMS

2.1 Preparation of Silica Monoliths

Silica monoliths with various pore sizes were synthesized through sol-gel method, following the works of [1] for nanofoams with the average pore size smaller than 500 nm and [2-4] for foams with larger average pore size, e.g. 1 μm , respectively.



(a) Nanopores



(b) Microscopic pores

Fig. 2.1 Flow charts of silica monolith processing

For the former (smaller pores), as shown in Fig. 2.1 (a), Sigma-Aldrich Ludox HS-40 colloidal silica was mixed with PQ Kasil-1 potassium silicate solution in a flask under magnetic stirring for 30 min, with the mass ratio in the range from 1:99 to 40:60. A larger colloidal silica amount tended to cause a reduced pore size. A 25 wt% formamide solution, which was diluted in water with the mass ratio of 40:60, was slowly added into the silica-silicate mixture and vigorously mixed by a magnetic stirrer for 30 min.

For the latter (larger pores), as depicted in Fig. 2.1 (b), Sigma-Aldrich tetramethyl orthosilicate (TMOS, 98%) was added to a 0.01 M aqueous solution of acetic acid, and was thoroughly mixed in a flask under magnetic stirring for 30 min. In the acetic acid solution, Sigma-Aldrich polyethylene glycol (PEG, with the average molecular weight of 10,000) had been dissolved. The TMOS to PEG mass ratio varied from 3.0 to 7.2, so as to tailor the pore size.

The mixture was then transported into a polypropylene plastic vial, either a smaller one with the inner diameter of 35.6 mm and the height of 16.3 mm (for smaller pores) or a larger one with the inner diameter of 46.2 mm and the height of 21.6 mm (for larger pores). The silica gels were dried in a VWR 1330GM oven at 80 °C for 72 h, and were sintered in a box oven at 850 °C for 1 h. Fig. 2.2 shows the sol-gel synthesis setups.



(a) Sol-gel synthesis



(b) Plastic molds and silica monoliths

Fig. 2.2 Setups for processing silica monoliths

2.2 High-Temperature Post-Processing Treatment of Silica Monoliths

The silica monoliths had different average pore sizes and porosities. The pore size and the porosity were highly correlated, as shown in Fig. 2.4. In order to uncouple these two important parameters, specifically to vary the pore size in a broad range and simultaneously, to keep the porosity around

60%, a post-processing calcination (PPC) treatment was carried out in a MTI GSL-1700X horizontal tube furnace at selected temperatures (T_s) for 1 h. The PPC temperatures ranged from 850 °C to 1265 °C. The ramp rate was initially set as 3 °C/min to keep the total heating time relatively short; and when the temperature was less than 100 °C away from T_s , was reduced to 1 °C/min, to minimize over-shooting. In order to reduce the residual stress, the cooling rate was set to be 3 °C/min.

In Fig. 2.3, it can be seen that compared with the pore size, the porosity is much more sensitive to the PPC temperature. When the temperature is at the vicinity of the glass transition point, T_g , of amorphous silica ~1200 °C [5], the viscosity of silica is highly dependent on temperature, resulting in the steep variation of the porosity [6]. The relative mild change in the average pore size should be attributed to the balance between the reduction in smaller pores and the shrinkage of larger pores [6,7]. Fig. 2.4 shows that as the PPC temperatures were optimized for silica monoliths of various initial pore sizes, their porosities could be adjusted to a similar level, e.g. 60%.

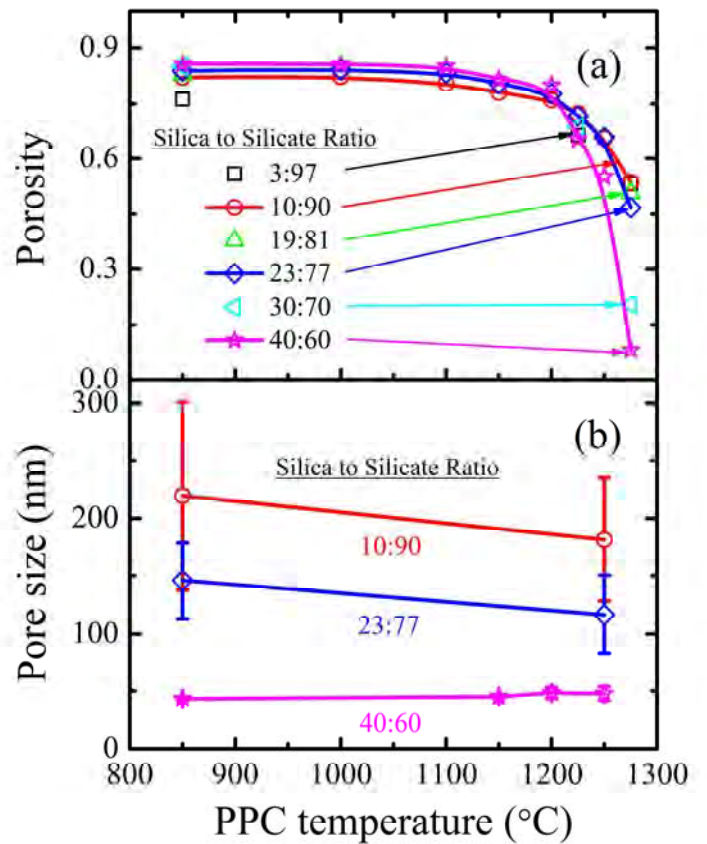


Fig. 2.3 Effects of the PPC temperature, T_s , on (a) the porosity and (b) the average pore size of silica nanofoams.

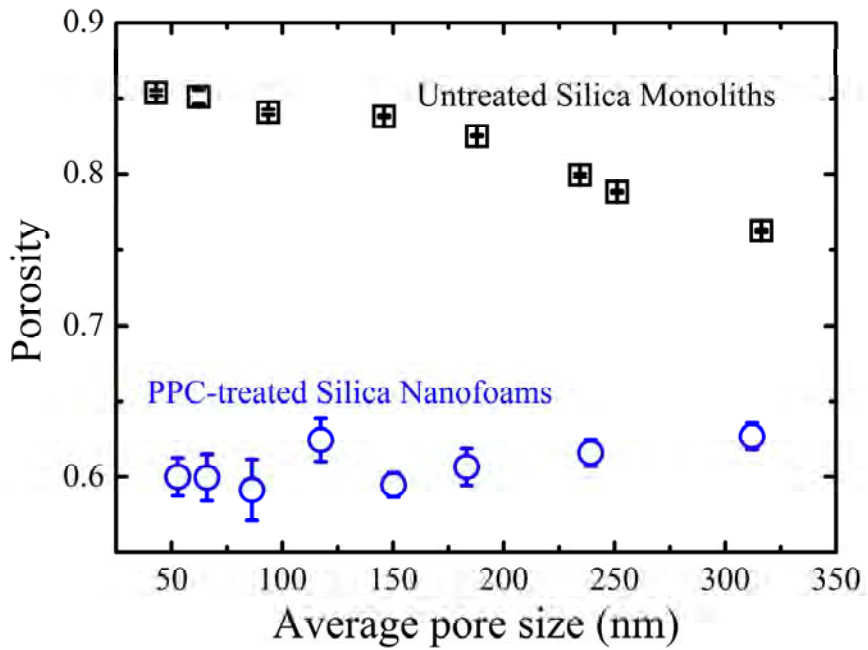


Fig. 2.4 Relationships between pore size and porosity of treated and untreated silicas.

2.3 Polishing of Silica Foams

To obtain homogeneous samples, the surface layers [8,9] of PPC-treated silica nanofoams were removed by a set of silicon carbide sandpapers. Before the PPC treatment, the thickness of the silica gel samples was 10-14 mm. After the PPC treatment, the thickness shrank to about 8-9 mm. Nearly 1.5 mm thick surface layers from the top and the bottom of the samples were first removed by 320-grit sandpapers, followed by further polishing with 600-grit sandpapers until the sample thickness was around 5 mm. Then, the sample thickness was reduced to about 4.75 mm by 1200-grit sandpapers and finally to about 4.50 mm by 2500-grit sandpapers. During the polishing, a self-made sample fixture, as shown in Fig. 2.5, was used to guarantee that the two sides of the sample disk were flat and in parallel, and that the final thickness had the accuracy of ± 0.05 mm.



Fig. 2.5 Sample fixture for polishing

2.4 Characterization of Silica Foams

2.4.1 Porosity

The porosities of the silica nanofoams were calculated from their mass densities [10]: $c = 1 - \rho/\rho_n$, where ρ is the sample density and $\rho_n = 2.2 \text{ g/cm}^3$ is the density of solid amorphous silica [6]. The specific pore volume is estimated using $v = c \cdot V_t/m$ [10], where V_t is the sample volume and m is the sample mass.

The dimensions and the porosities of PPC-treated silica foams are listed in Table 2.2. After being treated at different optimized PPC temperatures, the foams have a similar porosity ~60%, corresponding to a specific pore volume of ~ $0.7 \text{ cm}^3/\text{g}$.

2.4.2 Pore Size

The pore size (d) was characterized by the well-established Washburn method [11,12]: $d = 4\sigma \cos\theta/P_{Hg}$, where P_{Hg} is the infiltration pressure, $\sigma = 0.484 \text{ N/m}$ is the surface tension of mercury, and $\theta \sim 140^\circ$ is the contact angle. Fig. 2.6 shows typical mercury porosimetry curves of silica foams. The profile of the infiltration plateau, P_{Hg} , indicates the distribution of pore size. The width of the infiltration plateau is associated with the pore volume. The beginning and the ending points of the infiltration plateau are defined by dP/dV , as shown in Fig. 2.7. The beginning point is taken as the location where dP/dV abruptly drops, associated with the large decrease in effective system compressibility. The ending point is determined by the reference curve, 0.168 cm^3 away from the

peak loading. The average pore size is set as the average of the minimum and the maximum pore sizes determined from the infiltration plateau.

The mercury porosimetry results are summarized in Table 2.1. With the porosity ~60%, the average pore size of silica foams in the investigation ranges from tens of nm to more than 1 μm .

Table 2.1 Results of mercury porosimetry

Component mass ratio	TMOS to PEG 5.5:1.0	Colloidal silica to potassium silicate							
		1.3:98.7	7.5:92.5	12.5:87.5	17.0:83.0	22.5:77.5	27.5:72.5	35:65	40:60
PPC temperature ($^{\circ}\text{C}$)	1230	1260	1262	1260	1258	1254	1251	1239	1228
Mercury infiltration pressure range (MPa)	[0.75,1.89]	[3.85,6.21]	[5.06,8.01]	[6.71,10.20]	[8.45,11.87]	[10.96,14.93]	[14.77,20.55]	[19.37,26.80]	[24.45,32.91]
Pore size range (nm)	[780,1980]	[240,390]	[190,290]	[150,220]	[130,180]	[100,140]	[70,100]	[60,80]	[40,60]

Table 2.2 List of parameters of PPC-treated nanofoams

Average pore size (nm)	1380	315	240	185	155	120	85	70	50
Diameter (mm)	22.9 \pm 0.9	22.6 \pm 0.1	22.3 \pm 0.3	22.6 \pm 0.4	22.6 \pm 0.2	23.5 \pm 0.3	23.0 \pm 0.3	23.7 \pm 0.5	24.2 \pm 0.3
Thickness (mm)	4.51 \pm 0.02	4.51 \pm 0.01	4.53 \pm 0.01	4.51 \pm 0.01	4.53 \pm 0.01	4.53 \pm 0.01	4.51 \pm 0.01	4.52 \pm 0.01	4.52 \pm 0.01
Porosity (%)	59.6 \pm 2.7	62.7 \pm 0.9	61.6 \pm 0.9	60.7 \pm 1.2	59.5 \pm 0.8	62.4 \pm 1.4	59.1 \pm 2.0	60.0 \pm 1.5	60.0 \pm 1.3
Specific pore volume (cm ³ /g)	0.71 \pm 0.12	0.76 \pm 0.03	0.73 \pm 0.03	0.70 \pm 0.04	0.67 \pm 0.02	0.76 \pm 0.05	0.66 \pm 0.06	0.68 \pm 0.04	0.68 \pm 0.04

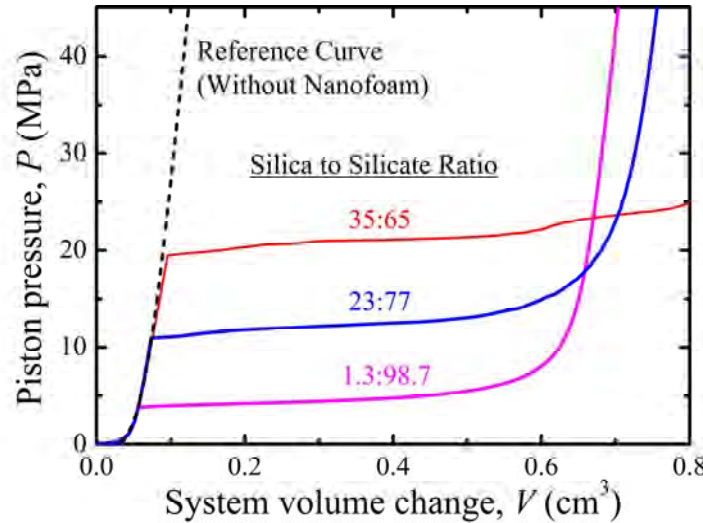


Fig. 2.6 Typical sorption isotherm curves of mercury porosimetry. The dashed curve is for the reference compression test on mercury, without any nanofoam.

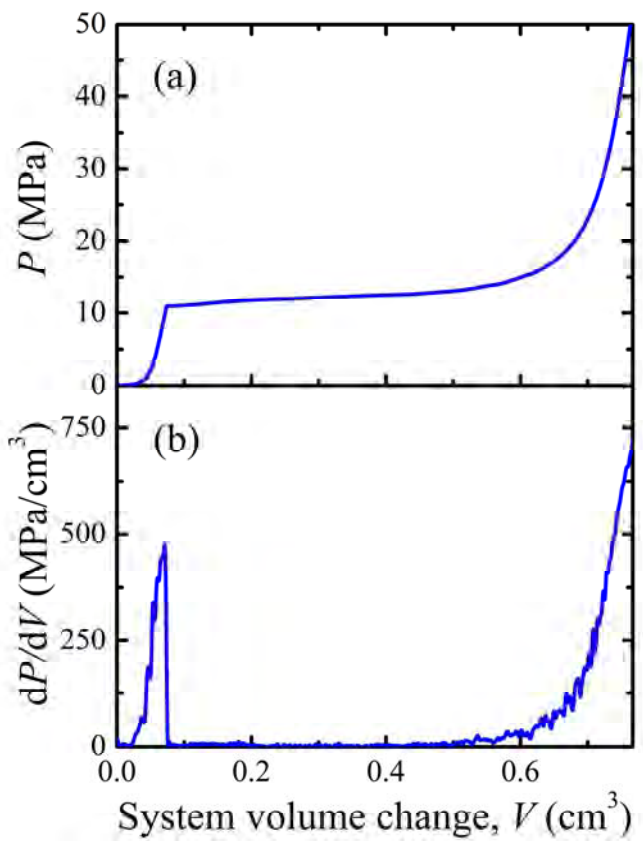


Fig. 2.7 Definition of the infiltration plateau: (a) a typical sorption isotherm curve showing the relationship between P and V ; (b) dP/dV .

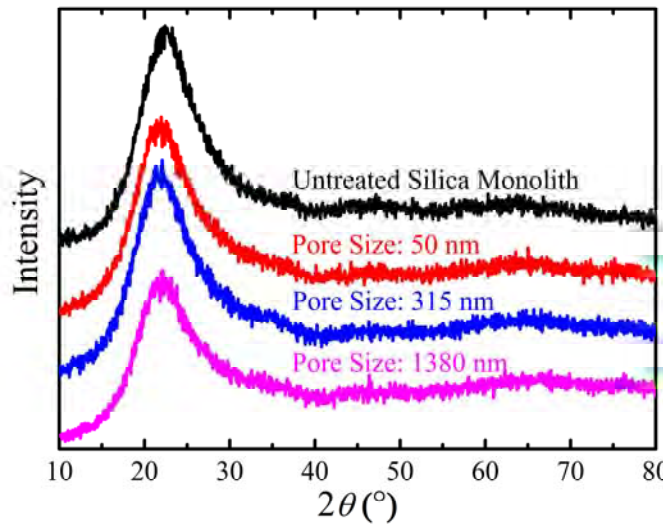


Fig. 2.8 Typical XRD analysis results. The top curve is for an untreated silica monolith, and the bottom three are for PPC-treated nanofoams.

2.4.3 Phase

The PPC-treated silica nanofoams were analyzed through powder x-ray diffraction, by using a Bruker D8 Advance Diffractometer at 40 kV and 40 mA for Cu K α ($\lambda = 1.5418 \text{ \AA}$). The scan speed was 0.1 sec/step; the step size was 0.02°; the 2 θ range was 10° to 80°.

As shown in Fig. 2.8, the broad peaks around $2\theta \approx 22^\circ$ suggest that the PPC-treated silica nanofoams all exhibit a short range order; that is, the PPC temperature, T_s , does not have any detectable influence on their amorphous nature.

2.4.4 Morphology

The silica nanofoams were also observed under a FEI-XL30 environmental scanning electron microscope (SEM) at 20kV, with a spot size of 3.0. The SEM samples had been coated with iridium using an Emitech K575X sputter coater at 85 mA for 6 seconds prior to the observation.

Fig. 2.9 confirms that the porous configurations of PPC-treated silica nanofoams are similar. As the pore size changes in a broad range, not only the porosity, but also the porous structure is not affected. All the pores are interconnected and open. The ligament length is correlated with the pore size, as it should be.

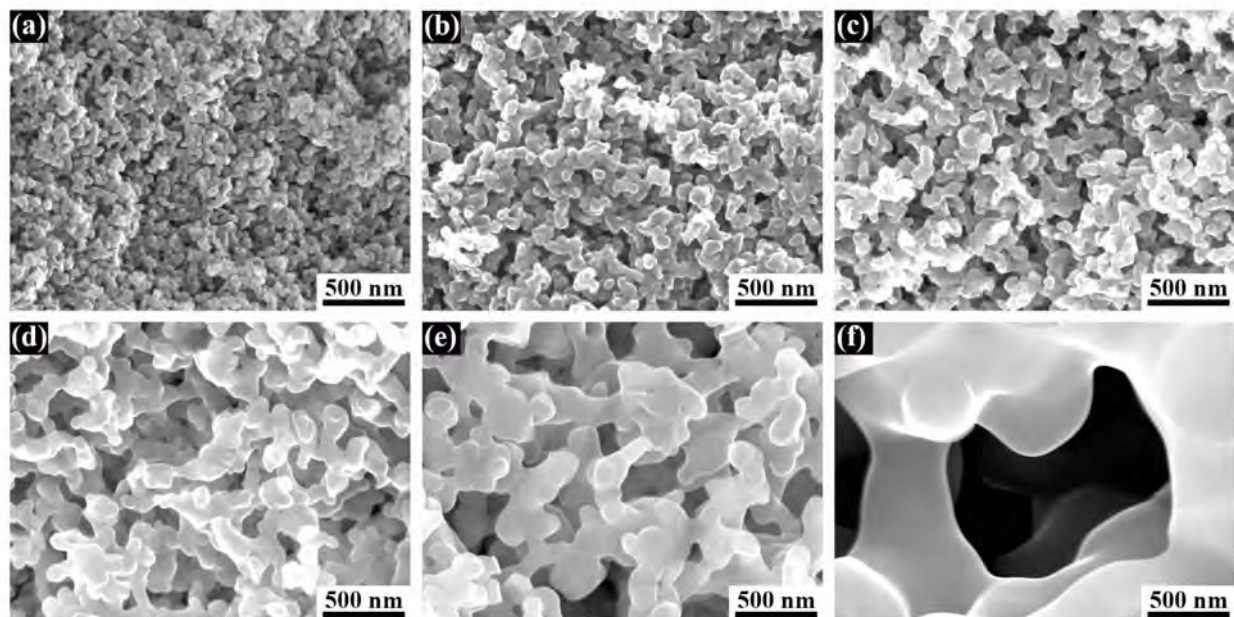


Fig. 2.9 Typical SEM images of PPC-treated silica nanofoams, with the average pore sizes of (a) 50 nm; (b) 85 nm; (c) 120 nm; (d) 185 nm; (e) 315 nm, and (f) 1380 nm. The porosities of all the silica nanofoams are ~60%.

3. DEVELOPMENT OF TESTING SYSTEMS

3.1 Development of Split Hopkinson Bar System

The dynamic responses of nanofoam disks of various pore sizes were characterized by a Split Hopkinson Bar (SHB) system, as depicted in Fig. 3.1 (a). By using a gas chamber, a Grade 9 titanium (Ti) tube striker was projected onto the impact end of the stainless steel incident bar. The outer diameter, the inner diameters, and the length of the striker were respectively 12.7 mm, 11.4 mm, and 462.0 mm. The two ends of the Ti tube were sealed by two 17-4 PH H900 stainless steel endcaps, respectively. The endcaps were pressed into the tube with a tight fit, and fixed by two stainless steel pins across the tube wall, respectively. The thickness of the endcaps was 5.1 mm, and the pin diameter and length were 3.2 mm and 12.7 mm, respectively. The striker was hosted by an AeroMarine polyurethane foam sleeve inside the gas chamber. The inner pressure in the gas chamber was fixed at 15.0 psi, leading to a nearly constant striker speed of 8.6 ed of 8.6oThe striker speed was measured by a couple of OMRON EE-SPW421 photomicro sensors.

The diameters of the incident bar and the transmission bar were the same, $D = 12.7$ mm; the lengths of them were 178 cm and 152 cm, respectively. They were made of 17-4 PH H900 stainless steel. The Youngunhe Youngtriker speGPa, and the density was 7750 kg/cm^3 . Two sets of Vishay WK-13-250BF-10C stain gauges were mounted on the center of the two bars, respectively, so as to measure the profiles of stress waves, through a Vishay 2310B data acquisition system (DAS).

To ensure that only a single pulse loading would be applied on the silica nanofoam sample, a momentum trapper was employed, following the works of [13,14], as shown in Fig. 3.1 (c). It consisted of a rigid block, a flange attached to the impact end of the incident bar, and a two-piece thread clamping locknut. There was a gap between the flange and the rigid block. The gap width was precisely controlled so that the motion of the flange would be stopped immediately after the whole tensile stress wave generated by the striker had entered into the incident bar. Thus, repeated pulse loadings were prevented.

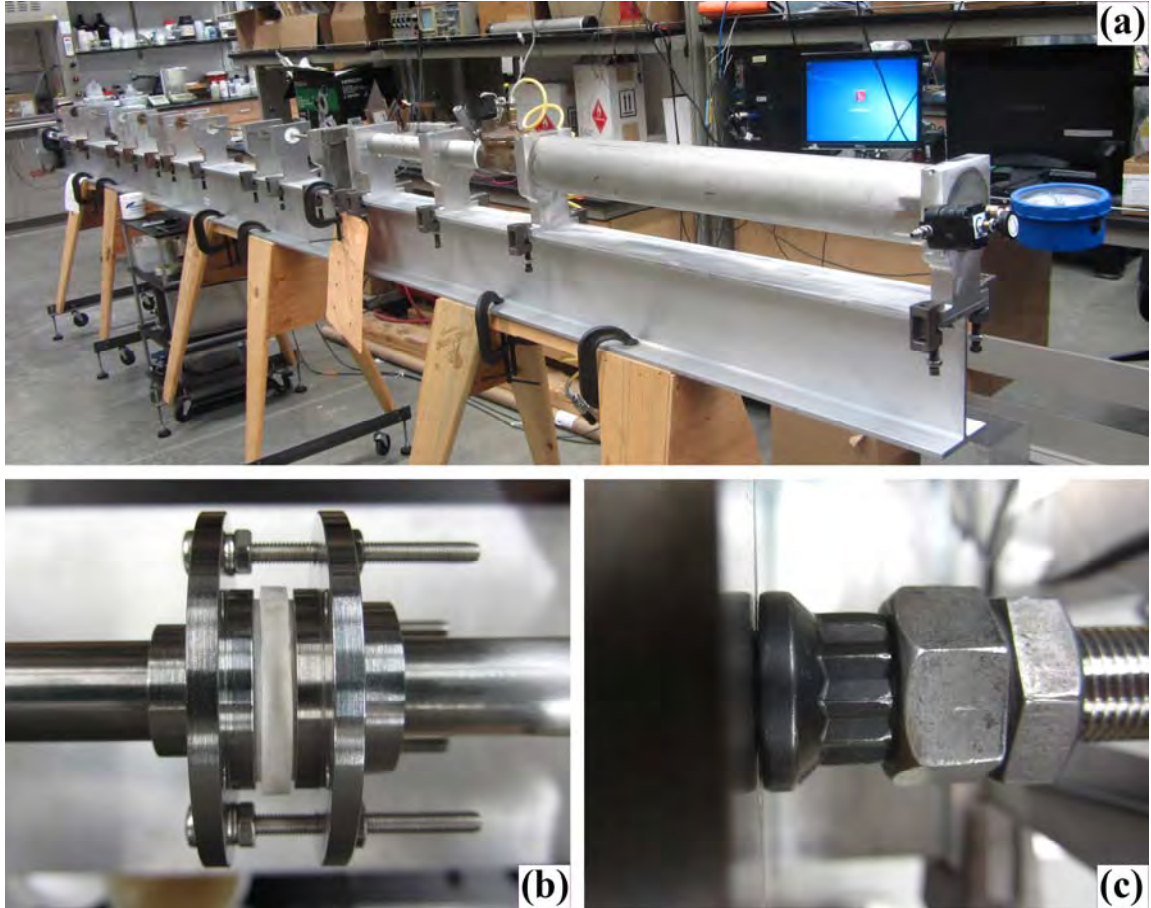


Fig. 3.1 Split Hopkinson Bar Systems: (a) the overall configuration; (b) the shear-promotion holder; and (c) the momentum trapper.

3.2 Development of Shear Promotion Holder

The shear promotion holder (SPH), as shown in Fig. 3.2, included a front part, a rear part and several mounting parts (e.g. cap screws, spring washers and hex nuts). The main body (rear and front parts) was made of 17-4 PH stainless steel. Fig. 3.3 showed its configuration in the SHB system. In Fig. 3.3 (a), the silica foam disk (#2) was mounted between the front part (#7, #8 and #9) and the rear part (#3, #4 and #6). The end of the incident bar (#1) was compressed against the surface of the sample. At the back of the silica disk, a stainless steel ring (#3) and a stainless steel disk (#4) were used to support the nanofoam sample against the transmission bar (#5). The inner diameter of the ring (#3, D_r) was 13.1 mm; the outer diameter was 25.0 mm; the thickness was 3.0 mm. The diameter of the steel disk (#4) was 43.0 mm; the thickness was 3.0 mm. The centers of the incident bar (#1) and the support ring (#3) were accurately aligned with the help of the designed parts (#6 and #9) and the tight fit between the six positioning holes (diameter 3.0 mm) on the edge of the SPH and the six corresponding M3 screws, with the gap width between the outer surface of

the incident bar (#1, D) and the support ring (#3, D_r) being 0.20 mm along all the directions. The parts (#3 and #7) were designed to reduce the potential bending of the nanofoam sample during the testing. Fig. 3.3 (b) sketched the working principle of the SHP. With the forces of the incident bar and the support ring applied on the nanofoam sample in the opposite directions, geometrical instability would be generated, promoting the development of the shear deformation. The design of SPH was inspired by the hat-shaped samples used by Marc Meyers and Vitali Nesterenko [15-17]. The lateral surface of nanofoam sample was loosely confined by a very soft polyurethane ring, with the initial inner diameter of 19.1 mm and outer diameter of 22.2 mm.

3.3 Quasi-static Shear Tests

At a constant rate of 0.01 mm/min, forced shear tests on silica foams were conducted using an INSTRON 5582 machine (Fig. 3.4). A 17-4 PH stainless steel rod with the diameter of 12.7 mm and the length of 25.4 mm was employed as the moving rod. The experimental configuration was identical to the SHB sample mounting setup. The shear gap width, i.e. the difference between the radius of the moving rod and the inner radius of the support ring, was 0.2 mm.



Fig. 3.2 The shear promotion holder and a silica foam disk sample.

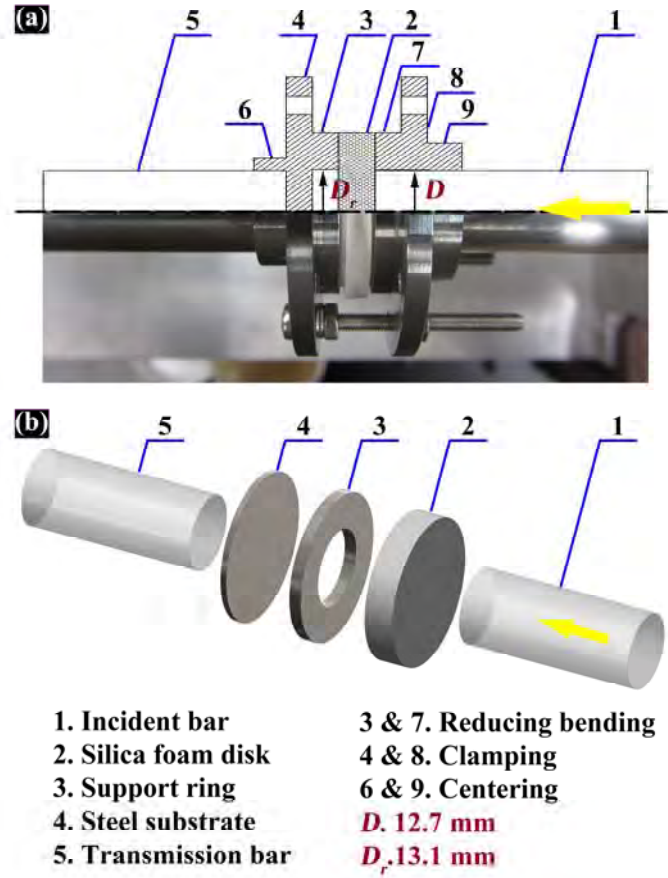


Fig. 3.3 Configuration of shear promotion holder in Split-Hopkinson bar: (a) half-section view of SPH; (b) diagram of forced shearing. The shear gap width here is 0.20 mm. The yellow arrow indicates the impact direction of the striker (not shown here).

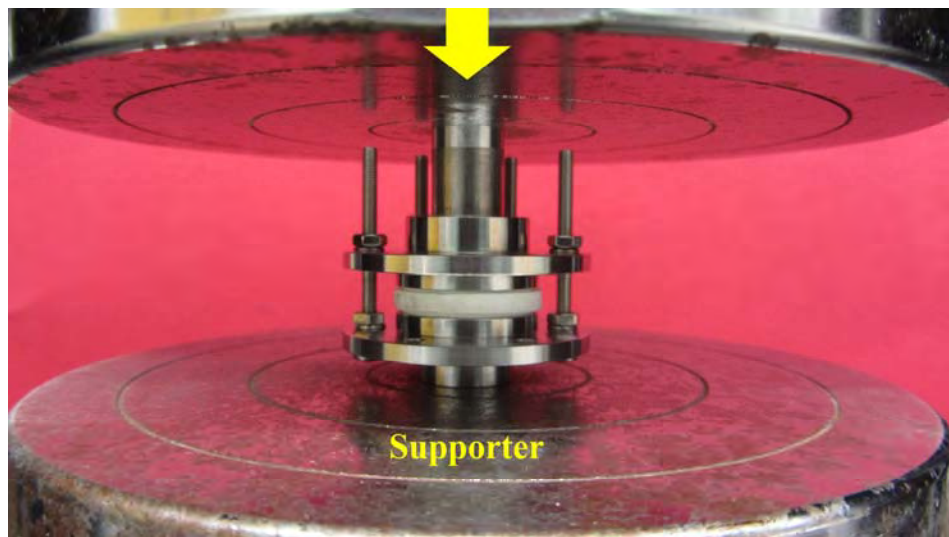


Fig. 3.4 Quasi-static shearing setups. The yellow arrow indicates the moving direction of the top end disk of the INSTRON.

3.4 Dynamic Compression Tests

Silica foams were directly sandwiched between the incident bar and the transmitted bar of the SHB system, and dynamic compression tests were performed. The silica foam samples were identical to that of quasi-static and dynamic shear tests.

3.5 Dynamic Shear Tests

In Fig. 3.5, silica foams with the average pore size ranging from tens of nm to more than 1 μm were forced-sheared on the shear promotion holder. For two-parameter testing, with both of the average pore size and the porosity varying in broad ranges (i.e. the silica foam samples were not PPC-treated), the shear gap was set to 0.2 mm, and the impact speed of titanium tube striker was 4.0 ± 0.5 m/s. For single-parameter testing, with the average pore size being the only variable (i.e. the silica foam samples were PPC-treated), the shear gap width ranged from 0.1~0.4 mm, and the impact speed was in the range of 5.0 ± 0.5 to 9.5 ± 0.5 m/s. For each type of foam, 3-5 samples were tested. The shear gap was defined as the difference between the radius of punch head and the inner radius of support ring.



Fig. 3.5 Dynamic shearing setups. The yellow arrow indicates the impact direction of the striker (not shown).

4. QUANTITATIVE SEM IMAGE ANALYSIS

To accurately measure the deformed zone size of silica foam sample after the dynamic shear test, we developed a quantitative image analysis technique using Matlab and Image-Pro Plus.

4.1 Two Dimensional Nominal Porosity

A scanning electron microscope (SEM) is employed to examine the microstructure of silica foams. Because the depth of the view field is larger than the pore size of the foams, there would be shadows in SEM images, as shown in Fig. 4.1 (b).

In order to carry out a quantitative image analysis, image filtering was conducted through a method combining the Shading Correction technique developed by Reyes-Aldasoro [18] and the Local Equalization function provided by the Image-Pro Plus software (Media Cybernetics Manufacturing, Warrendale, PA, USA), as demonstrated in Fig. 4.2. A SEM image was first enhanced by the Shading Correction, reducing the shadow of the pore structure. Then it was imported into Image-Pro Plus and Local Equalization was employed to enhance its local contrast with the window size of 60 pixels, the step of 1 pixel and the standard deviation of 0.5. Finally the Otsu's method [19] was used to obtain the threshold (Matlab built-in function Graythresh) and the image was converted into binary format, as shown in Fig. 4.2 (c).

On the converted image, the white areas were considered as pore walls and the black zones were taken as pores. Therefore, a nominal two-dimensional porosity ($AP2$) was defined as the fraction of the white area. The measurement results of $AP2$ qualitatively matched the porosity data calculated from mass density (ρ) and were consistent for self-comparison purpose. The numbers of pixels in white and black areas were counted through the Matlab built-in function Bwarea.

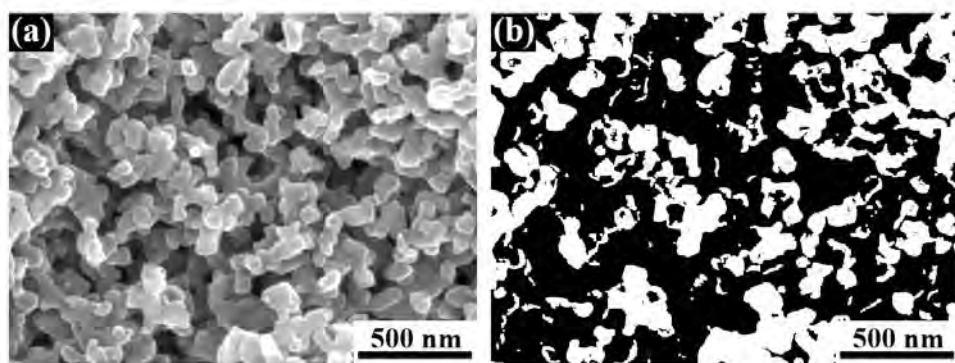


Fig. 4.1 Shadow in the SEM image of a silica foam: (a) an original SEM image; (b) a final binary image.

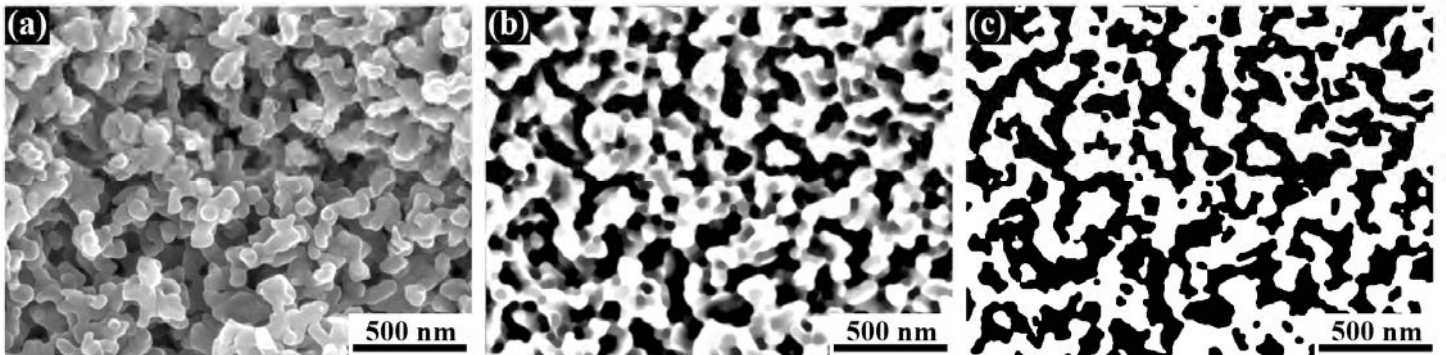


Fig. 4.2 Two dimensional nominal porosity of a silica foam: (a) a typical original SEM image; (b) an enhanced SEM image; and (c) a binary image derived from the Otsu's method ($AP2 = 0.515$).

4.2 Harvesting SEM Samples

4.2.1 Low impact velocity tests

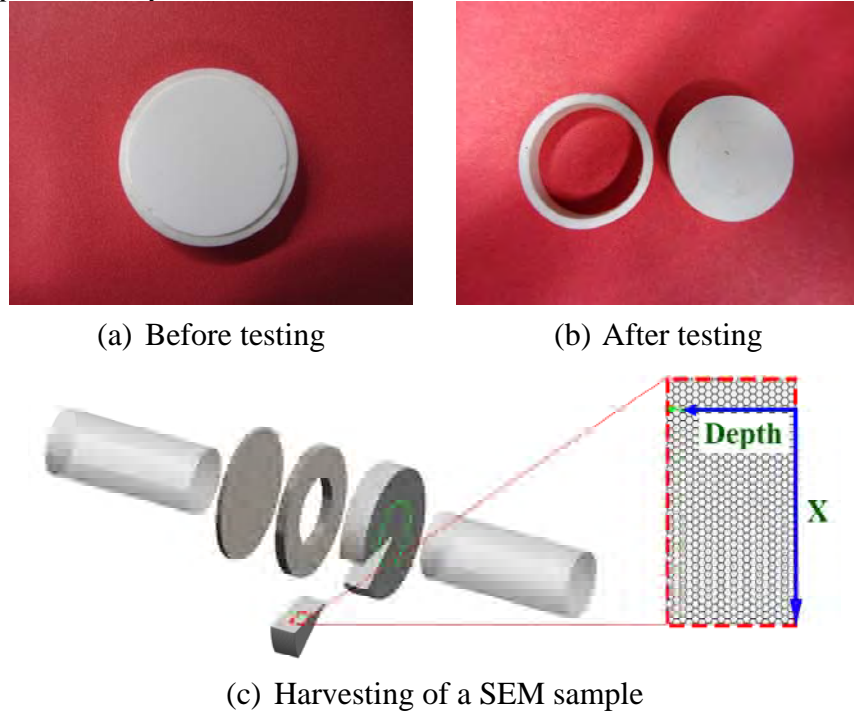


Fig. 4.3 Forced-sheared silica foam under the impact speed of 4 m/s.

After the SHB testing, SEM samples were harvested from the impacted silica foam disks. Under a low impact velocity, as depicted in Fig. 4.3, the silica foam sample remained structurally integral after testing. Attention was primarily focused on the front side of the silica foam disk facing the incident bar. To best preserve useful information, a thin layer of epoxy was applied on all the other sides of the disk. From the back surface, in the center part of the disk and along a straight line, three holes with the diameter of 0.0236'' were drilled. A razor blade was placed in the middle hole, with the sharp corner toward an adjacent hole, and was carefully impacted by a hand hammer. A

crack would generated and propagated along the line of the three holes, splitting the foam disk in two equal parts. The exposed lateral fresh fracture surfaces were observed by SEM.

4.2.2 High impact velocity tests

At a relatively high impact velocity, after testing, the silica foam disk would fragment into a number of smaller pieces, as shown in Fig. 4.4. The parts of the least crack density should contain the most information that we were interested in, and thus were chosen for the SEM analysis. Note that the origin in SEM image needs to be offset, as the central part of the disk is lost (Fig. 4.4 (a)).

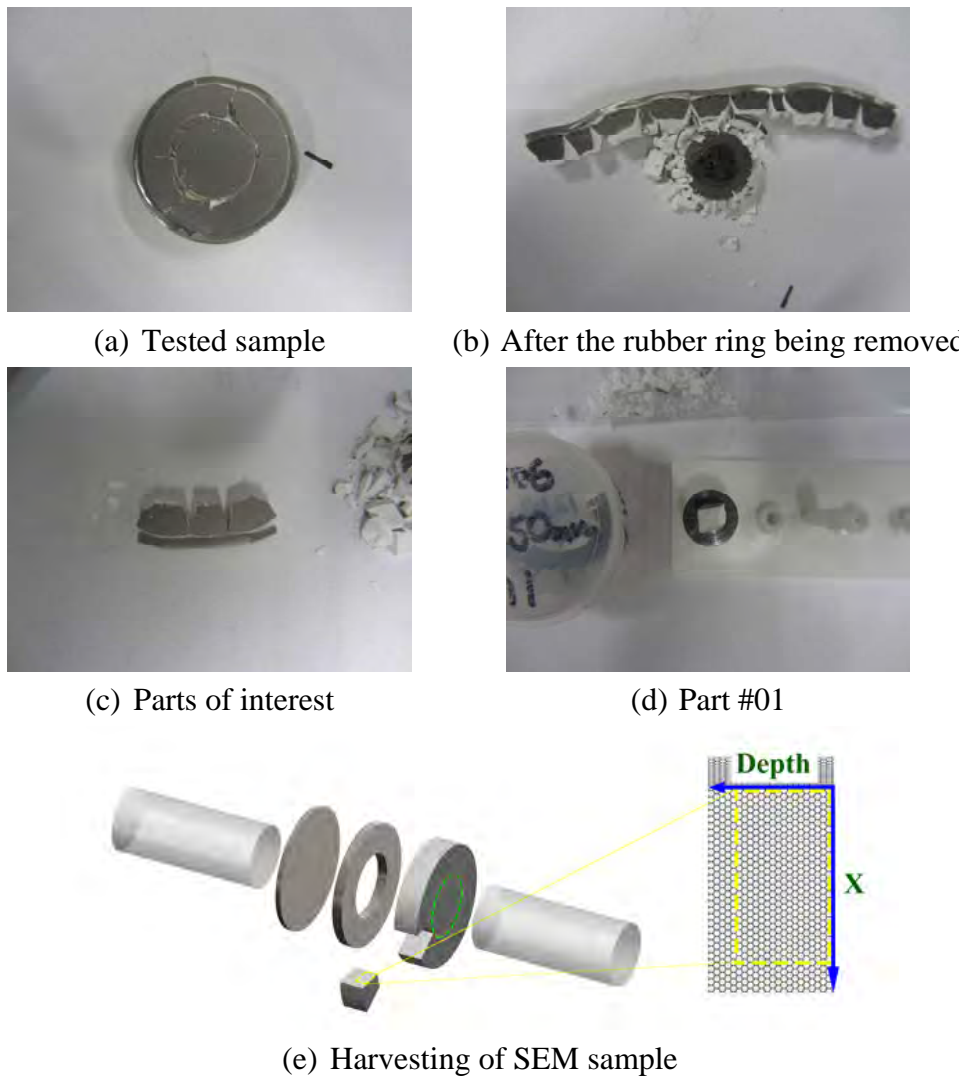


Fig. 4.4 Forced-sheared silica foam under the impact speed of 8.5 m/s. The dark color on the surface of the SEM sample is caused by the iridium coating.

4.3 Strategy of SEM Scanning

A relatively large number of SEM images were analyzed. To best observe the information of deformation zones, the preserved sample surfaces were strategically scanned.

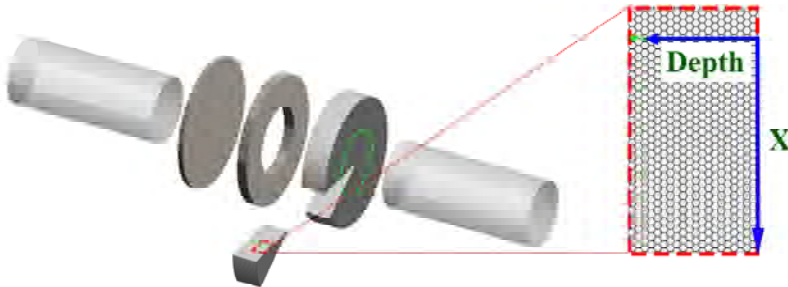
First, we assessed the scanning range of the foam sample through visual inspection. The primary goal was to determine the areas of deformed pores. As the pore size was small and the number of pores was large, the boundaries of deformation zones could be calculated only based on statistics. As shown in Fig. 4.5 (a), the areas around the intersection of the edge of the incident bar and the front surface of the foam disk should be scanned. Because the sections immediately adjacent to the sample-bar interface might have been compressed and were very often damaged, the relatively far fields were given a higher priority.

Second, we built up an X-D coordinate system, with “D” indicating the sample depth direction (parallel to the impact direction) and “X” the radius direction (normal to the impact direction). The origin was set at the intersection of the edge of incident bar and the front surface of foam sample, based on surface features. The X-D coordinate helped locate the scanning points and coordinate the analysis results of different fields.

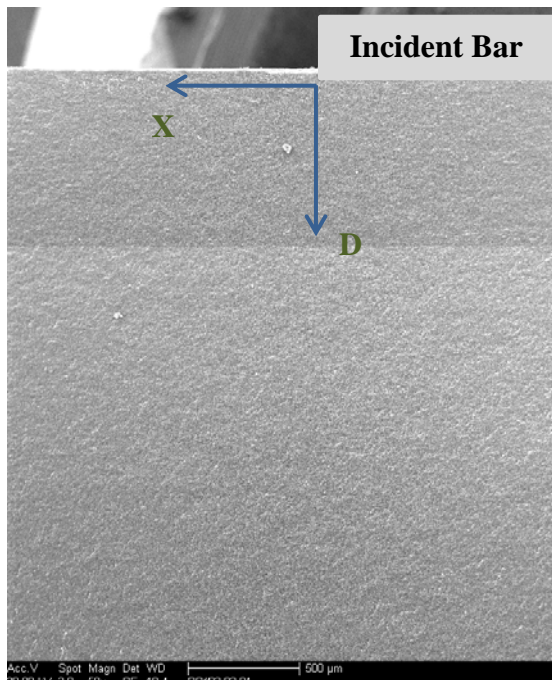
Third, we set a scanning map. For each SEM sample, relatively large square field ahead of the origin was scanned; typically, ~600 images were taken, corresponding to ~100 scanning points. Usually five or six scanning lines were needed to give an acceptable resolution of the boundary of deformation zone. One line was for the compressed area, and the rest were for the elastic area. About 20 points along each line were observed. The sample thickness was 5.00 mm or 4.50 mm. To cover a half of the thickness by 20 points, the distance between adjacent scanning points (D_1) should be about 125 μm . In our work, for the sake of convenience, D_1 was set to 186 μm at the magnification of 500X, the same as the height of a single SEM image. Trivial areas (e.g. cracks or damaged spots) might be skipped occasionally.

Then, we set the scanning path for each scanning point, so that the SEM view field returned to the starting spot after six images were taken.

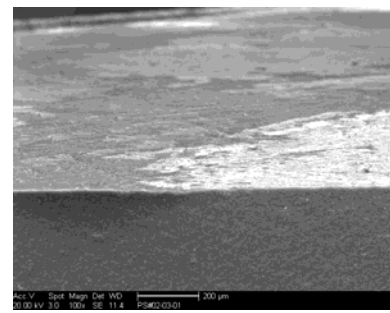
Finally, we took high-resolution SEM images following the pre-set path for each scanning point. This scanning strategy, specified in Table 4.1, must be strictly followed for all scanning points for all the SEM samples.



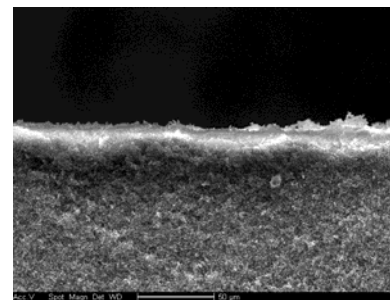
(a) Schematic of the scanning range



(b) A larger view



(c) Surface features



(d) A starting point

Fig. 4.5 SEM scanning strategy

Table 4.1 SEM scanning strategy

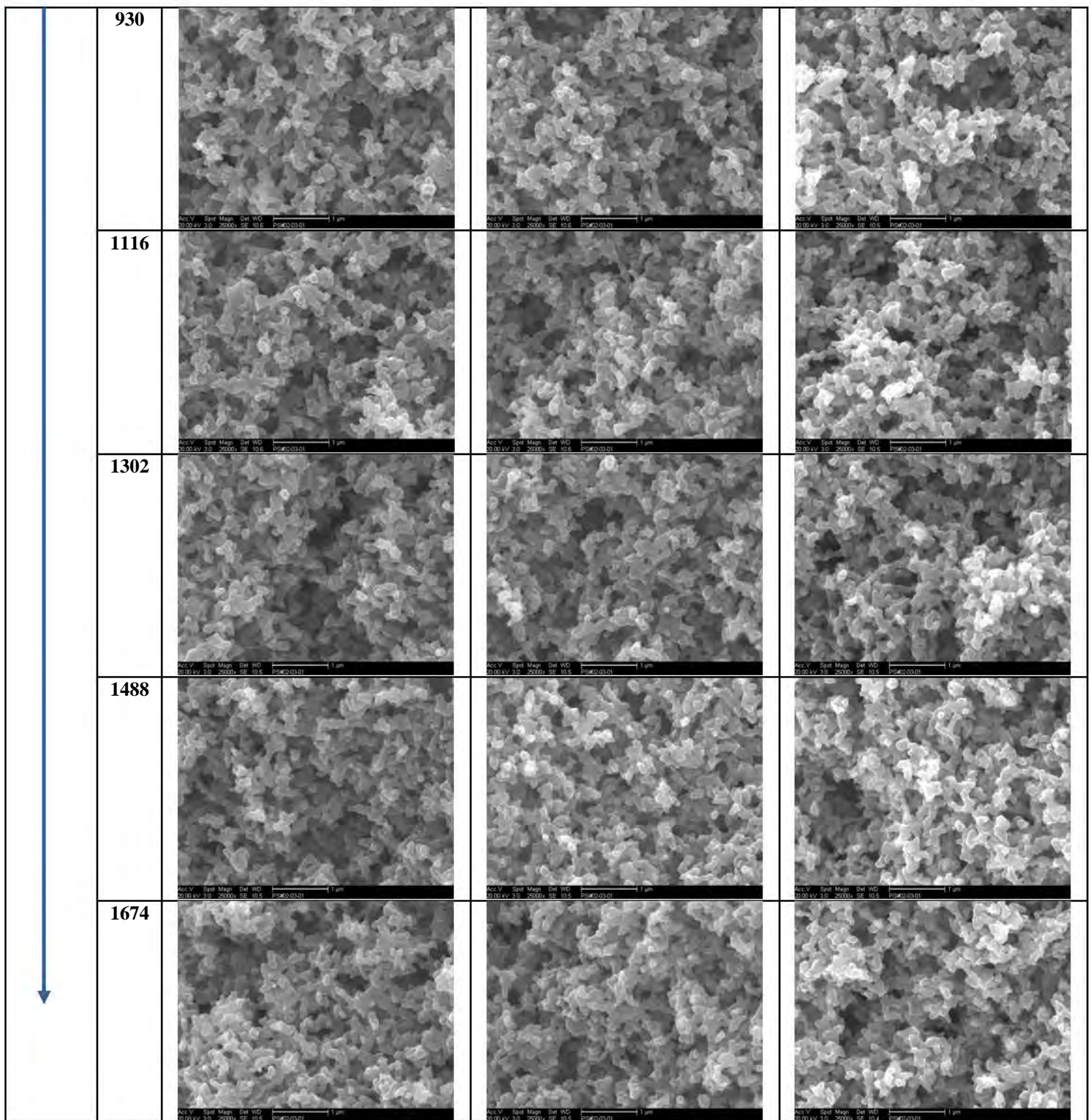
(50 X **2.42 mm** × **1.86 mm**; 500 X **242 μm** × **186 μm**; 25000 X **4.84 μm** × **3.72 μm**)

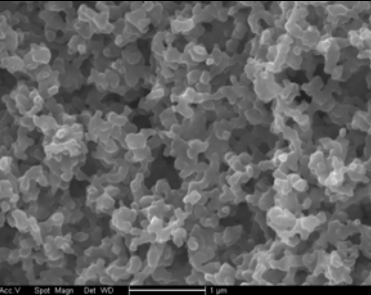
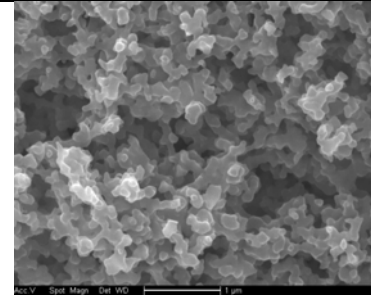
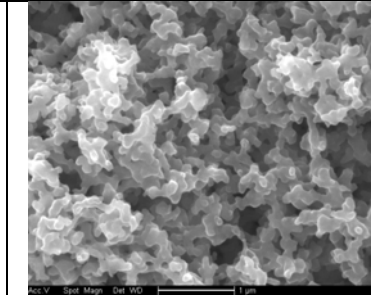
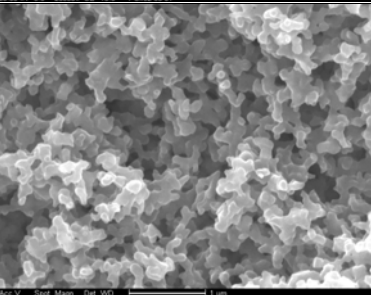
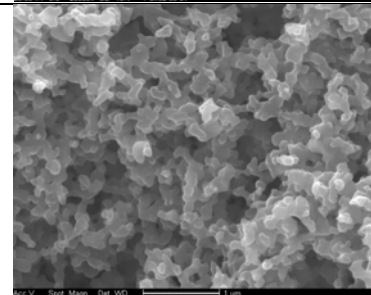
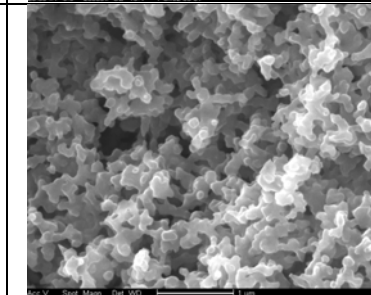
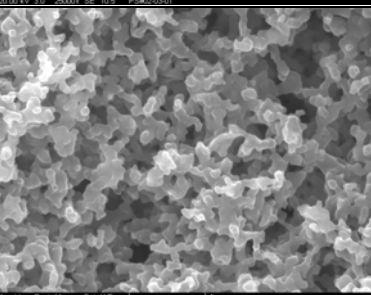
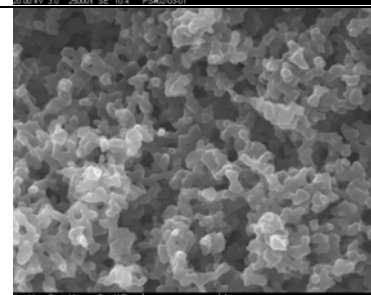
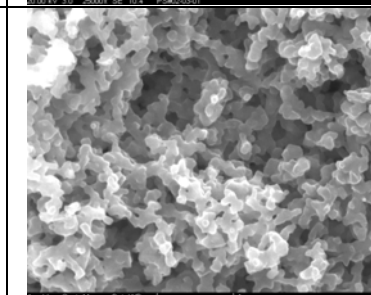
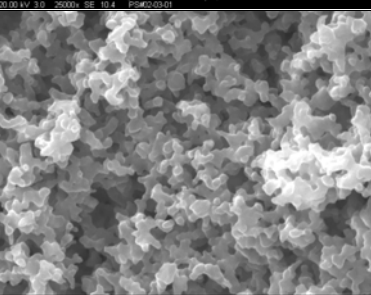
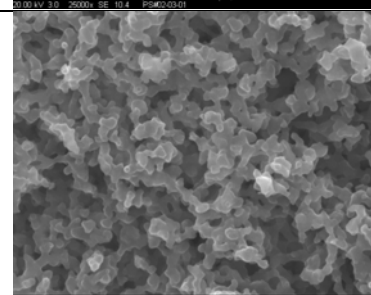
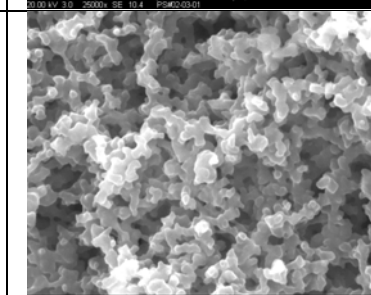
	Non-compression zone				Starting Point			Compression zone
X D	968	726	484	242	0			-242
0					5	4	3	
					6	1	2	
186								
372								
558								
744								

Table 4.2 Original SEM images of scanning lines

(Sample thickness 5.00 mm; pore size 255 nm; porosity 78.8%)

Unit: μm		X ←	484	242	0
Depth ↓	0				
	186				
	372				
	558				
	744				



	1860			
	2046			
	2232			
	2418			
Depth				

Depth				

Table 4.3 An example of the results of SEM image analysis
 (Sample thickness 5.00 mm; pore size 255 nm; porosity 78.8%;
 partition 3×3 ; critical value 0.532)

Unit: μm	X												
		968	Stdev	726	Stdev	484	Stdev	242	Stdev	0	Stdev	-242	Stdev
Depth	0	0.5375	0.0145	0.5399	0.014	0.5438	0.0172	0.5382	0.0138	0.5335	0.0114	0.5307	0.0143
	186	0.528	0.0171	0.531	0.0149	0.5281	0.011	0.54	0.0118	0.5304	0.0134	0.5241	0.0149
	372	0.5312	0.0153	0.5317	0.0146	0.5261	0.0126	0.5315	0.0111	0.5354	0.0136	0.5291	0.0174
	558	0.5239	0.0149	0.5252	0.0147	0.529	0.0127	0.5345	0.0177	0.5308	0.0194	0.5233	0.0132
	744	0.5236	0.0121	0.5292	0.0161	0.5227	0.0148	0.5383	0.0155	0.5195	0.012	0.5355	0.0205
	930	0.5305	0.0151	0.5305	0.0167	0.5232	0.0172	0.5221	0.0147	0.5306	0.0129	0.536	0.0115
	1116	0.5353	0.0118	0.5232	0.0147	0.5277	0.0171	0.5284	0.0189	0.5312	0.0121	0.5325	0.0135
	1302	0.5273	0.0128	0.529	0.0176	0.5242	0.0176	0.5209	0.0171	0.5223	0.015	0.5246	0.0171
	1488	0.5361	0.0156	0.5329	0.0143	0.5394	0.013	0.5283	0.0129	0.5394	0.0125	0.5244	0.0151
	1674	0.5285	0.0152	0.5266	0.0186	0.5363	0.0177	0.5246	0.0146	0.5233	0.011	0.529	0.017
	1860	0.5299	0.0163	0.5311	0.0184	0.5187	0.0171	0.5252	0.0193	0.5384	0.0137	0.5228	0.013
	2046	0.5273	0.0161	0.5329	0.0163	0.5253	0.0213	0.512	0.014	0.5199	0.013	0.5214	0.0123
	2232	0.5283	0.0147	0.5198	0.0112	0.5263	0.0153	0.5214	0.0205	0.532	0.0167	0.5311	0.0127
	2418	0.5226	0.0184	0.5268	0.0125	0.5331	0.0177	0.5213	0.0169	0.526	0.0165	0.5169	0.0146

Table 4.4 Updated results of SEM image analysis
 (Sample thickness 5.00 mm; pore size 255 nm; porosity 78.8%;
 partition 3×3 ; background porosity: 0.5246; critical value 1.014)

Unit: μm	X						
		968	726	484	242	0	-242
Depth	0	1.0246	1.0292	1.0366	1.0259	1.0170	1.0116
	186	1.0065	1.0122	1.0067	1.0294	1.0111	0.9990
	372	1.0126	1.0135	1.0029	1.0132	1.0206	1.0086
	558	0.9987	1.0011	1.0084	1.0189	1.0118	0.9975
	744	0.9981	1.0088	0.9964	1.0261	0.9903	1.0208
	930	1.0112	1.0112	0.9973	0.9952	1.0114	1.0217
	1116	1.0204	0.9973	1.0059	1.0072	1.0126	1.0151
	1302	1.0051	1.0084	0.9992	0.9929	0.9956	1.0000
	1488	1.0219	1.0158	1.0282	1.0071	1.0282	0.9996
	1674	1.0074	1.0038	1.0223	1.0000	0.9975	1.0084
	1860	1.0101	1.0124	0.9888	1.0011	1.0263	0.9966
	2046	1.0051	1.0158	1.0013	0.9760	0.9910	0.9939
	2232	1.0071	0.9909	1.0032	0.9939	1.0141	1.0124
	2418	0.9962	1.0042	1.0162	0.9937	1.0027	0.9853

4.4 Image Analysis

Using the developed quantitative image analysis technique, the distribution of local nominal porosity for each selected sample was measured, based on two assumptions: (a) the pore structure along the line of $X = 0$ undergoes the most evident deformation, and (b) the cell buckling is less pronounced in the far field. A critical local porosity change ratio, above which the pore structure is considered deformed, is used to define the boundary of the deformation zone: $\beta = (\text{local porosity})/(\text{reference porosity})$, where the reference porosity is the average porosity of non-deformed areas (far fields from the origin). Due to the small pore size and the large pore number, the standard deviation in the measurement of local porosity is quite small, less than 5% of the average porosity.

Take the silica foam sample with the average pore size of 255 nm as an example. Table 4.2 shows the original SEM images along the scanning lines, $X = 0 \mu\text{m}$, $X = 242 \mu\text{m}$ and $X = 484 \mu\text{m}$. The image analysis results are listed in Table 4.3. The background porosity is measured as 0.5246, and the critical normalized porosity, β , is 1.014. Table 4.4 gives the updated image analysis results, in which the deformed zone is marked by the red numbers.

5. TWO-PARAMETER STUDY ON SILICA FOAMS

Without the PPC treatment, the pore size and the porosity of silica foams are correlated: A foam of a higher porosity tends to have a smaller pore size. According to conventional dynamic mechanics, a foam with a lower porosity should have a higher shear strength, and thus, the pressure of transmitted stress wave of such a sample tends to be higher. Is it true? It will be shown below that our testing data on two-parameter nanofoams are contradictory to this prediction.

5.1 Two-parameter Silica Foams

After calcination at 850 C for 1 hour, the pore size of silica foam was characterized by mercury porosimetry, and the porosity was calculated from the mass density. The results are listed in Table 5.1. The porosity varies from 76.2% to 88.1%, and the average pore size ranges from tens of nm to more than 1 μm .

Table 5.1 List of the parameters of two-parameter silica foams

Component mass ratio		Thickness (mm)	Porosity (%)	Pore size range (nm)	Average pore size (nm)
TMOS to PEG	5.1:1.0	5.03 \pm 0.01	88.1 \pm 0.1	[1170,1770]	1470
Colloidal silica to potassium silicate	3 : 97	5.03 \pm 0.02	76.2 \pm 0.1	[240,390]	315
	10 : 90	5.03 \pm 0.01	79.9 \pm 0.1	[180,290]	235
	15 : 85	5.04 \pm 0.02	82.1 \pm 0.1	[160,280]	220
	17 : 83	5.04 \pm 0.01	82.5 \pm 0.1	[140,230]	185
	19 : 81	5.05 \pm 0.01	82.9 \pm 0.1	[140,200]	170
	23 : 77	5.05 \pm 0.01	83.8 \pm 0.1	[120,170]	145
	25 : 75	5.05 \pm 0.01	84.1 \pm 0.1	[90,100]	95
	30 : 70	5.03 \pm 0.01	85.1 \pm 0.2	[59,65]	62
	40 : 60	5.04 \pm 0.03	85.6 \pm 0.1	[42,44]	43

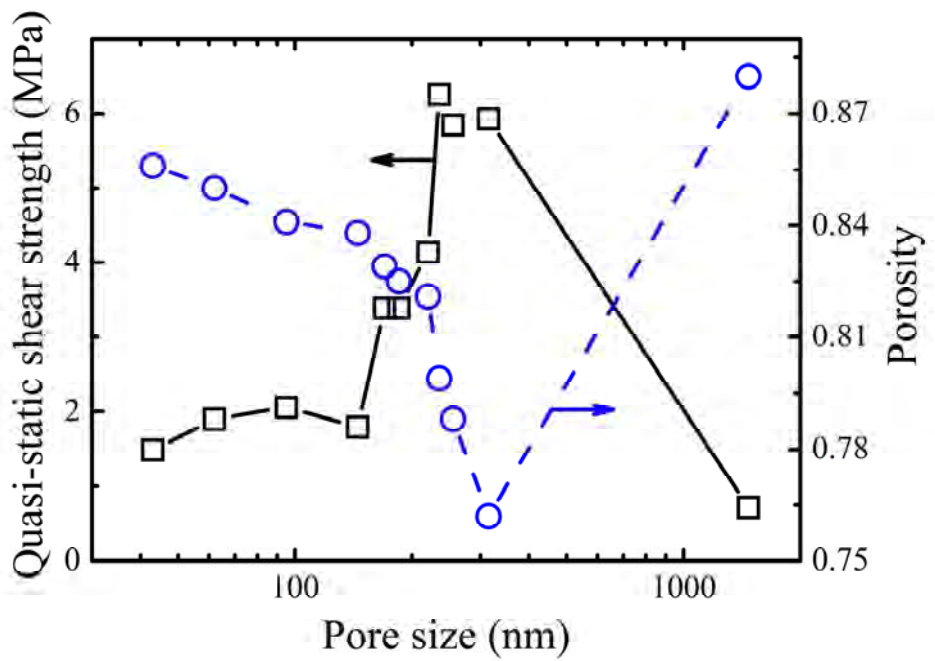


Fig. 5.1 Results of quasi-static shear tests on two-parameter silica foams.

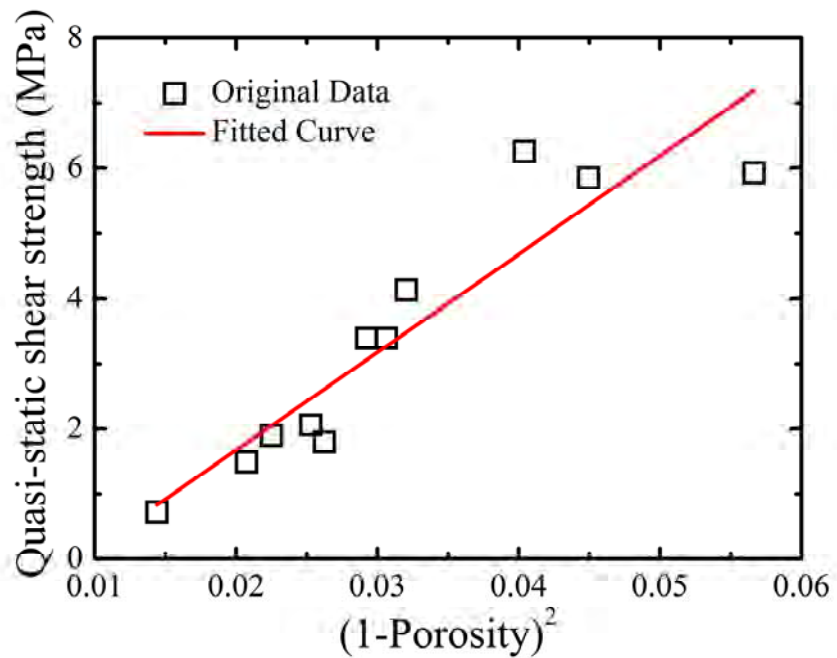


Fig. 5.2 Quasi-static shear strength of two-parameter silica foams as a function of the porosity.

5.2 Quasi-static Shear Tests

Quasi-static shear tests on non-PPC treated, two-parameter silica foams were conducted using an INSTRON 5582 machine, with the loading rate of 0.01 mm/min. The shear gap width was set to 0.20 mm. In Fig. 5.1, it can be seen that a foam with a lower porosity tends to have a higher quasi-static shear strength (S). For instance, the sample with the porosity of 88.1% has a quasi-static shear strength of 0.72 MPa; the sample with the porosity of 76.2% has a much higher shear strength, nearly 6.0 MPa. That is, the quasi-static shear strength is highly sensitive to the porosity.

Consider a foam with open cells. The shear strength can be assessed as $S = A \cdot (1-p)^2$, where A is a constant and p is the porosity [10]. As shown in Fig. 5.2, the regressed curve according to this theory matches well with the testing data, and the value of $A = 151 \pm 21$ MPa. It may be concluded that the quasi-static shear strength of a foam is highly dependent on its porosity, while relatively unrelated to the pore size.

5.3 Dynamic Shear Tests

Two-parameter silica foams with the average pore size ranging from tens of nm to more than 1 μm were forced-sheared in the SHB system, with the aid of the shear promotion holder. The shear gap width was 0.20 mm and the titanium-tube striker velocity was 4.0 ± 0.5 m/s.

As shown in Fig. 5.3, after the test, the silica foam samples remained structurally integral, without extensive cracking.



(a) Before testing

(b) After testing

Fig. 5.3 Two-parameter silica foams before and after SHB shearing. The white ring in the right photo is the rubber holder.

Fig. 5.4 shows typical signals collected by the strain gauges on the incident bar and the transmission bar. The relationship between the transmitted wave pressure ($P_{t,s}$) and the average pore size of two-parameter silica foams is shown in Fig. 5.5. With the similar incident wave pressure \sim 12-13 MPa, when the average pore size is reduced from more than 1 μm to tens of nm, the transmitted wave pressure increases first, and then drops, as predicted by the conventional mechanics, due to the change in porosity and in shear strength. However, when the average pore size is in the range of 170-315 nm, there is an abrupt drop in the transmitted wave pressure as the pore size is lowered; the transmitted wave pressure becomes smaller than the equivalent maximum normal stress ($P_{t,0}$) under quasi-static shearing. In another word, under dynamic shearing, the transmitted wave pressure is not only dependent on the porosity, but also related with the pore size of the foams. This pore size effect is contradictory to the continuum mechanics theory.

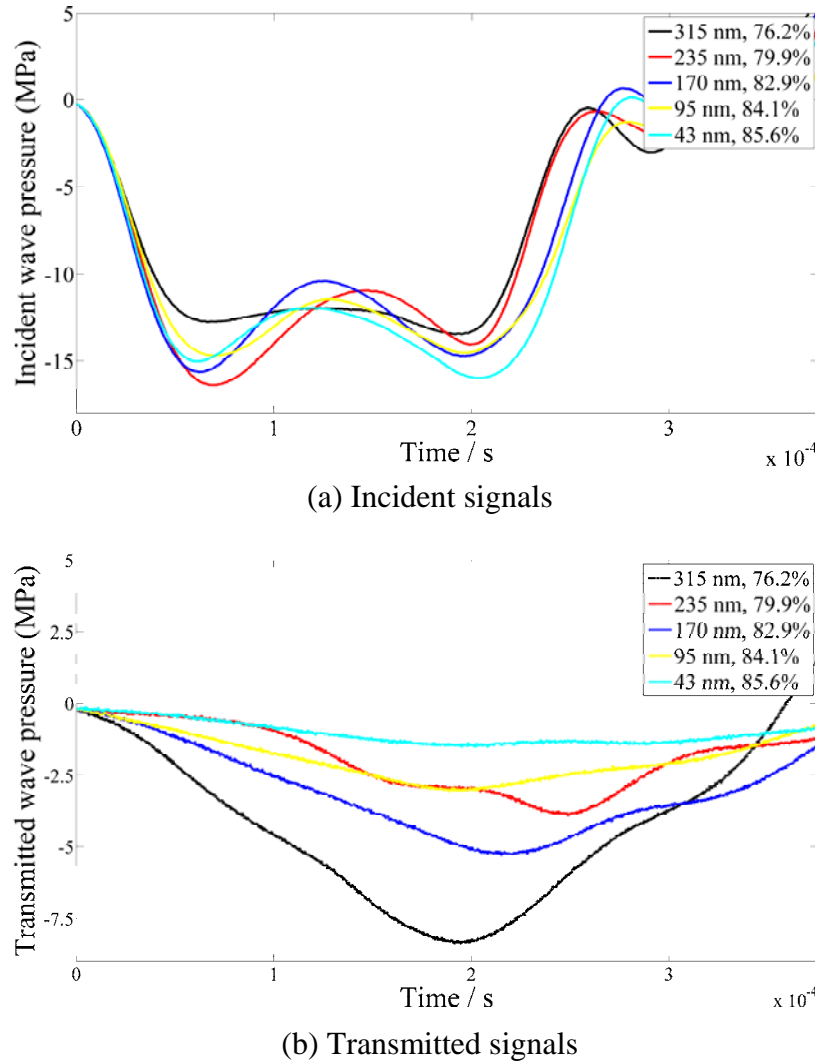


Fig. 5.4 Typical SHB shearing testing curves of two-parameter silica foams

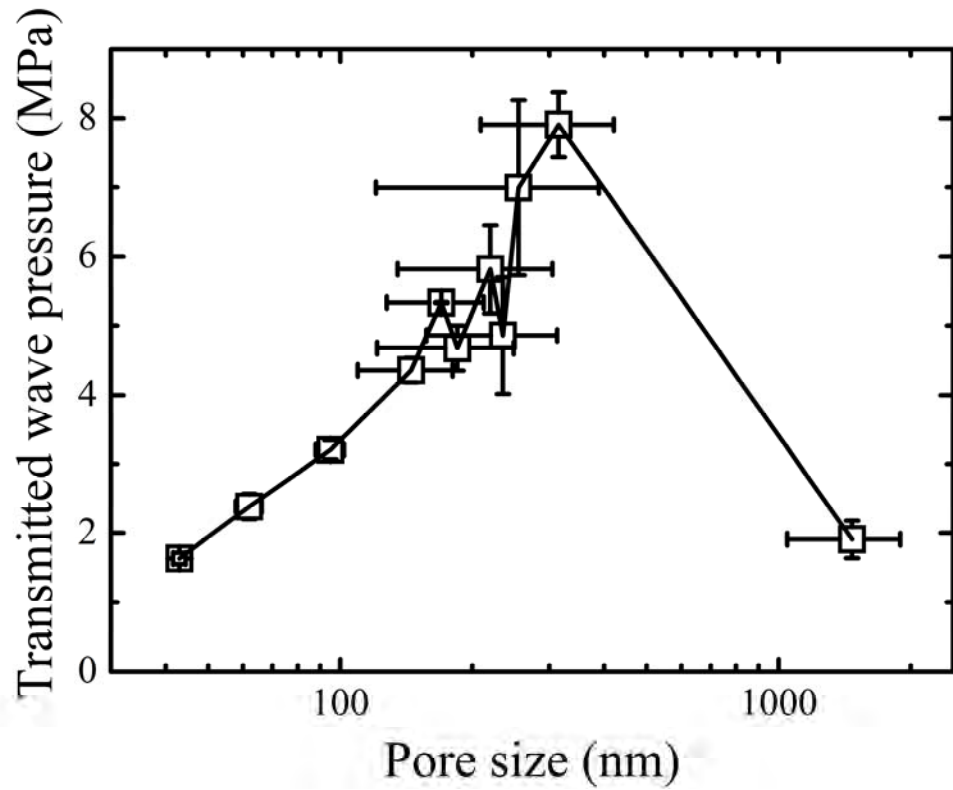


Fig. 5.5 Transmitted wave pressure of two-parameter silica foams

To make it more clear, the results of dynamic shearing and quasi-static shearing are combined in Fig. 5.6, where the pressure, instead of the shear strength, is examined. The equivalent maximum normal stress under quasi-static shear condition is the maximum force on the moving rod divided by the cross-sectional area. Obviously, when the pore size is within the median range, the maximum pressure under dynamic shearing is much smaller than that under quasi-static shearing. The maximum difference reaches ~ 5.0 MPa at the average pore size of 235 nm. Thus, under dynamic loadings, the effective shear strength is not only related to the porosity, but also dependent on the pore size.

Under the similar testing conditions (striker impact speed and shear gap width), it is the energy absorption that results in the reduction of the maximum pressure. For silica foams, the energy absorption is caused by cell collapse. The more volume of the foam involves in the cell collapse process, the more energy will be absorbed, and thus the lower the transmitted wave pressure will be. In another word, the amount of energy absorption of silica foams is a function of the average

pore size.

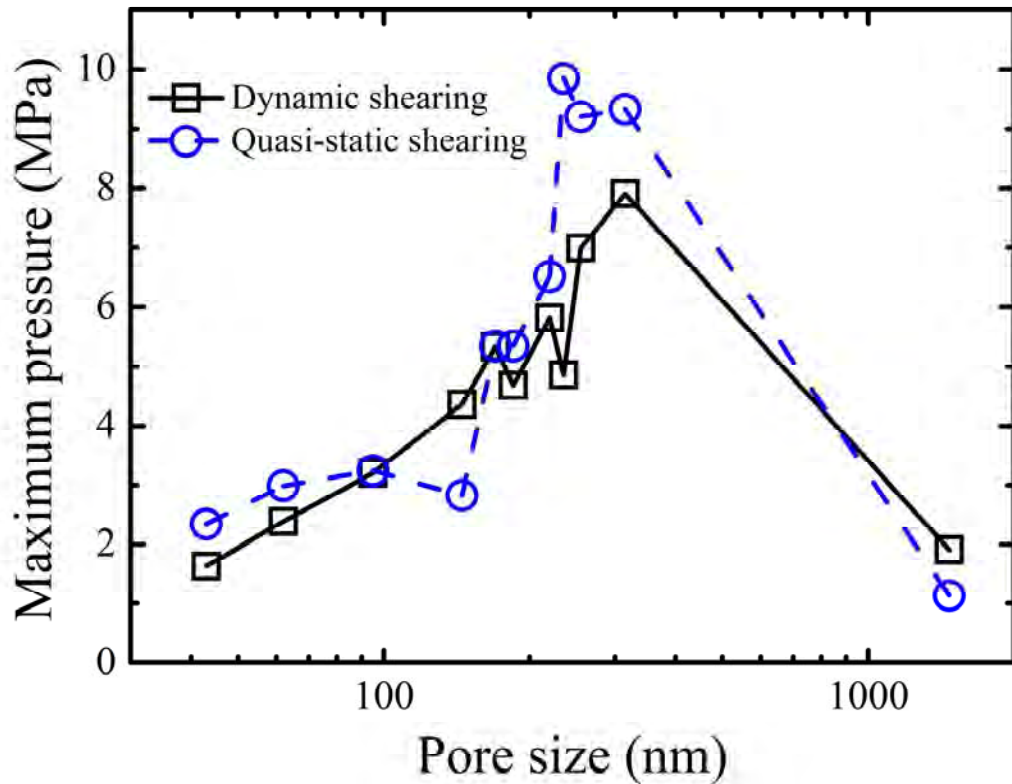


Fig. 5.6 Comparison between dynamic shearing and quasi-static shearing of two-parameter silica foams

5.4 Deformation Zone

In Fig. 5.7, the measured profiles of deformation zones are shown in the X-D coordinate system. Under the same criterion of β , the scanning points with higher normalized porosity values are marked by black squares; the red squares outline the boundary of the deformation zones.

When the average pore size is 315 nm, we can clearly see that the cell collapse was concentrated in a narrow band; when the pore size decreases to 235 nm, the damaged area becomes much broader, suggesting that the reduction in pore size tends to have a beneficial effect to promote widespread energy dissipation.

Table 5.2 shows the relationship between the pressure reduction of transmitted stress wave and the area of deformation zone. The silica foam with the average pore size of 235 nm exhibits the most

widespread cell collapse area, leading to the largest pressure reduction.

The experimental results of two-parameter silica foam samples indicate that: (1) as predicted by continuum mechanics, the quasi-static shear strength is a function of porosity and is quite insensitive to the pore size; (2) under a dynamic shear loading, the transmitted wave pressure is highly dependent on the pore size, especially when the pore size is in the nanoporous range around 200-300 nm.

However, because the pore size and the porosity are correlated in the two-parameter samples, it is difficult to specifically analyze the pore size effect, and therefore, the study is somewhat non-conclusive. In order to circumvent this problem, we developed the post-processing calcination (PPC) technique to decouple the pore size and the porosity, as discussed previously. The PPC-treated samples, which will be referred to as single-parameter foams, will be discussed in the following sections.

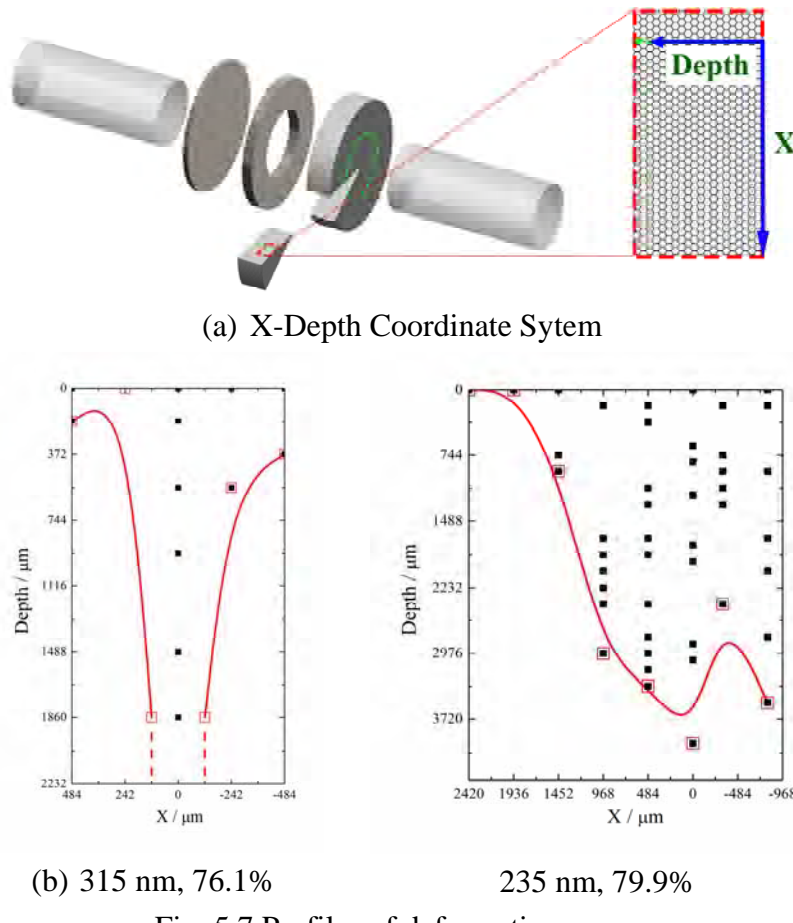
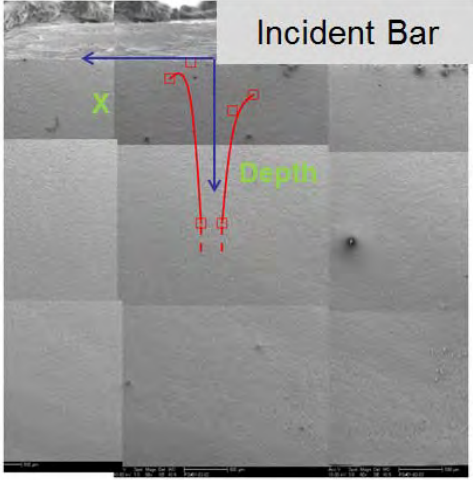
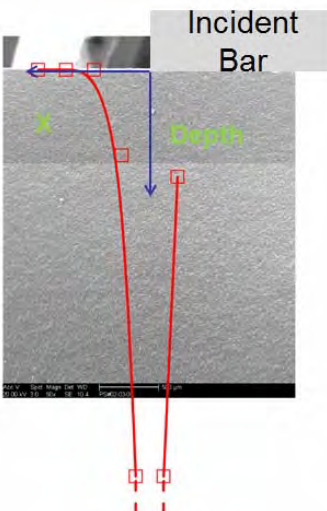
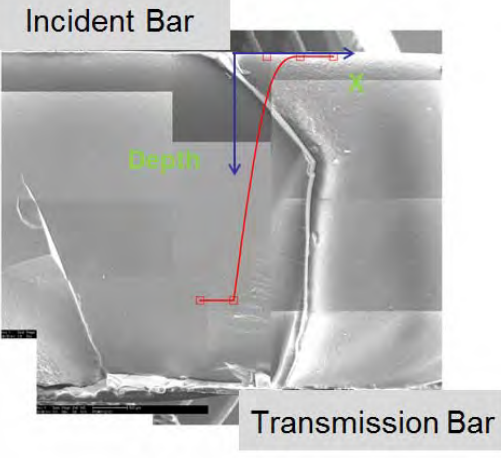
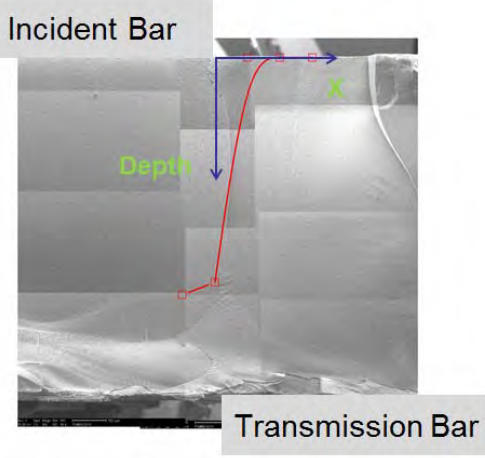


Fig. 5.7 Profiles of deformation zones.

Table 5.2 Summary of two-parameter testing

(a)		<p>Sample Information</p> <p>Average pore size: 315 nm Porosity: 76.1% Dimensions: D19.40 mm, T5.02 mm Quasi-static shear strength: 5.93 MPa Equivalent maximum normal pressure: 9.33 MPa</p> <p>Dynamic Shearing Results</p> <p>Average incident pressure: 12.08 MPa Transmitted pressure: 8.37 MPa Normalized transmitted pressure: 0.693 Pressure reduction: 0.96 MPa</p>
(b)		<p>Sample Information</p> <p>Average pore size: 255 nm Porosity: 78.8% Dimensions: D19.98 mm, T5.02 mm Quasi-static shear strength: 5.85 MPa Equivalent maximum normal pressure: 9.21 MPa</p> <p>Dynamic Shearing Results</p> <p>Average incident pressure: 10.73 MPa Transmitted pressure: 7.93 MPa Normalized transmitted pressure: 0.739 Pressure reduction: 1.28 MPa</p>

(c)	 <p>Incident Bar</p> <p>Depth</p> <p>Transmission Bar</p>	<p>Sample Information</p> <p>Average pore size: 235 nm Porosity: 80.0% Dimensions: D20.75 mm, T5.02 mm Quasi-static shear strength: 6.25 MPa Equivalent maximum normal pressure: 9.85 MPa</p> <p>Dynamic Shearing Results</p> <p>Average incident pressure: 12.89 MPa Transmitted pressure: 3.92 MPa Normalized transmitted pressure: 0.304 Pressure reduction: 5.93 MPa</p>
(d)	 <p>Incident Bar</p> <p>Depth</p> <p>Transmission Bar</p>	<p>Sample Information</p> <p>Average pore size: 185 nm Porosity: 82.5% Dimensions: D22.06 mm, T5.05 mm Quasi-static shear strength: 3.39 MPa Equivalent maximum normal pressure: 5.34 MPa</p> <p>Dynamic Shearing Results</p> <p>Average incident pressure: 13.21 MPa Transmitted pressure: 4.32 MPa Normalized transmitted pressure: 0.327 Pressure reduction: 1.02 MPa</p>
(e)	 <p>Incident Bar</p> <p>Depth</p> <p>Transmission Bar</p>	<p>Sample Information</p> <p>Average pore size: 170 nm Porosity: 82.9% Dimensions: D22.40 mm, T5.05 mm Quasi-static shear strength: 3.39 MPa Equivalent maximum normal pressure: 5.34 MPa</p> <p>Dynamic Shearing Results</p> <p>Average incident pressure: 12.98 MPa Transmitted pressure: 5.32 MPa Normalized transmitted pressure: 0.410 Pressure reduction: 0.02 MPa</p>

6. SINGLE-PARAMETER STUDY ON SILICA FOAMS

6.1 Single-parameter Silica Foams

After PPC treatment at different optimized temperatures for 1 h, the porosities of silica foams were adjusted to a similar level, ~60%, while their average pore sizes span from tens of nm to more than 1 μm . The XRD results (Fig. 2.8) indicate that the PPC temperature has little influence on the amorphous nature of silica foams. The SEM images (Fig. 2.9) show that all the foams have a similar morphology. The single-parameter sample information, including the thickness, the porosity, and the pore size range, is listed in Table 6.1.

Table 6.1 List of parameters of PPC-treated silica foams

Component mass ratio		Thickness (mm)	Porosity (%)	Pore size range (nm)	Average pore size (nm)
TMOS to PEG	5.5:1.0	4.51 \pm 0.02	59.6 \pm 2.7	[780,1980]	1380
Colloidal silica to potassium silicate	1.3:98.7	4.51 \pm 0.01	62.7 \pm 0.9	[240,390]	315
	7.5:92.5	4.53 \pm 0.01	61.6 \pm 0.9	[180,290]	240
	12.5:87.5	4.51 \pm 0.01	60.7 \pm 1.2	[150,220]	185
	17.0:83.0	4.53 \pm 0.01	59.5 \pm 0.8	[130,180]	155
	22.5:77.5	4.53 \pm 0.01	62.4 \pm 1.4	[100,140]	120
	27.5:72.5	4.51 \pm 0.01	59.1 \pm 2.0	[70,100]	85
	35:65	4.52 \pm 0.01	60.0 \pm 1.5	[60,80]	70
	40:60	4.52 \pm 0.01	60.0 \pm 1.3	[40,60]	50

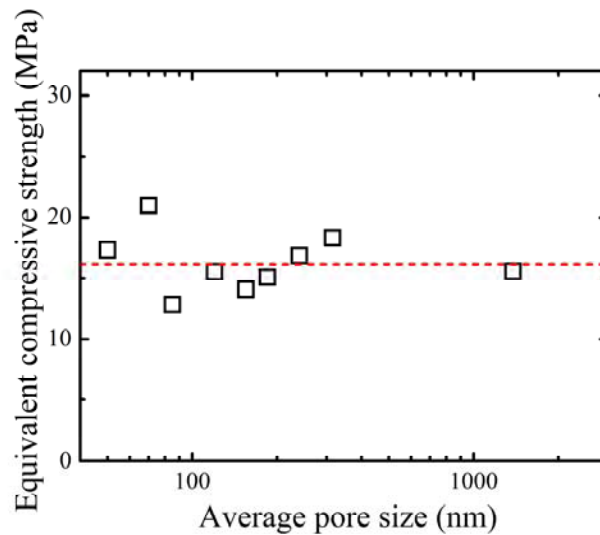


Fig. 6.1 Results of quasi-static shearing on PPC-treated silica foams. The red dash line gives the theoretical value of 16.1 MPa.

6.2 Quasi-static Shear Tests

Quasi-static shear experiment was conducted on PPC-treated, one-parameter silica foams using an INSTRON 5582 machine, with the loading rate of 0.01 mm/min. The shear gap width was set to be 0.20 mm. Fig. 6.1 shows the testing results.

For open cells, the quasi-static shear strength (the maximum quasi-static shear stress) of a foam follows the relationship: $S = B \cdot S_0 \cdot (1-p)^2$, where B is a constant, S_0 is the shear strength of solid material, and p is the porosity [10].

The shear strength of solid amorphous silica is ~70 MPa. Thus, for silica foams with porosity ~60%, the relative density is ~0.40 and the theoretical shear strength ~11.2 MPa ($B = 1$). The investigated sample thickness is ~4.50 mm; the diameter of the loading rod is 12.7 mm; the inner diameter of the support ring is 13.1 mm; thus, the equivalent compressive strength ($P_{t,0}$) is ~16.1 MPa. In Fig. 6.1, under the shear strain rate of $8.3 \times 10^{-4} \text{ s}^{-1}$, the equivalent compressive strengths of all the silica foams with the similar porosity of ~60% are around the predicted value of 16.1 MPa. Note that their pore sizes vary from 50 nm to 1380 nm.

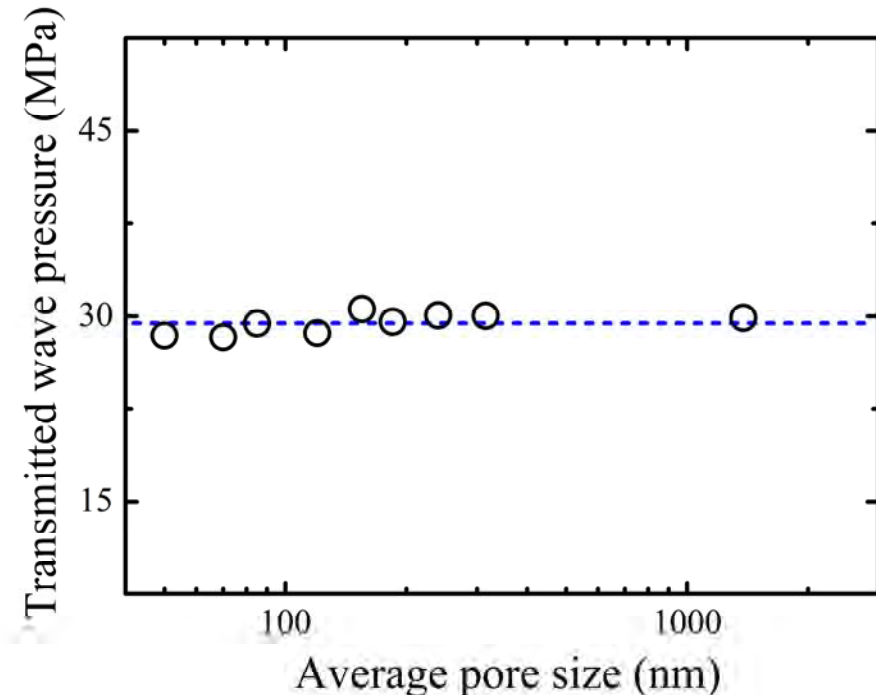


Fig. 6.2 Maximum transmitted wave pressure of PPC-treated silica foams, in dynamic compression test. The blue dash line indicates the average value of 29.4 MPa.

6.3 Dynamic Compression Tests

The silica foam samples were tested in the SHB system in a regular compressive wave setup. The sample was sandwiched in between the incident bar and the transmitted bar, and the incident and transmitted, one-dimensional compressive waves were measured by the strain gauges on the incident bar and the transmitted bar, respectively.

At an interface, the impedance mismatch determines the percentage of the energy that will be reflected. In Fig. 6.2, under the strain rate of $\sim 200 \text{ s}^{-1}$, the maximum transmitted wave pressure ($P_{t,c}$) is quite insensitive to the pore size of the foams, indicating that all the foams have a similar acoustic impedance.

6.4 Dynamic Shear Tests

Unlike the quasi-static shear or the dynamic compression tests, the maximum transmitted wave pressure of dynamic shear test ($P_{t,s}$) becomes highly sensitive to the pore size. The testing results were listed in Table 6.2.

6.4.1 *Transmitted wave pressure*

Fig. 6.3 gives the testing data collected by the strain gauges on the incident bar and the transmission bar.

Fig. 6.4 shows the maximum transmitted wave pressure as a function of the average pore size. Under the shear strain rate of 4500 s^{-1} , with the decrease of the average pore size, the maximum transmitted wave pressure first decreases, and then exhibits a lower plateau at about 100-200 nm.

6.4.2 *Pressure Reduction*

With the theoretical quasi-static value, 16.1 MPa, as a reference, the relative variation of the maximum transmitted wave pressure is defined as $|\xi| = |P_{t,s} - P_{t,0}|/P_{t,0}$. It can be seen in Fig. 6.5 that (1) when $\xi > 0$ (ξ^+), the maximum transmitted wave pressure is higher than 16.1 MPa; this region is defined as the Regular Region; and (2) when $\xi < 0$ (ξ^-), the maximum transmitted wave pressure is lower than 16.1 MPa; this region defined as the Nano Region, a new size effect is evident.

6.4.3 Energy Absorption

Under the similar shear strain rate of $\sim 4500 \text{ s}^{-1}$, the transmitted wave energy (U_t), as shown in Fig. 6.6 (a), exhibits a similar trend as the transmitted wave pressure, as the pore size varies from the Regular Region to the Nano Region.

The energy absorption efficiency (η) can be defined as [20]: $\eta = (U_i - U_r - U_t)/(U_i - U_r)$, where U_i , U_r and U_t are the total energy carried by the incident, reflected and transmitted pulses respectively. The wave energy consists of a strain energy part (U_s) and a kinetic energy part (U_k): $U = U_s + U_k = \kappa \int_0^T \sigma^2(t) dt$, where $\sigma(t)$ is the wave pressure, t is time, and $\kappa = A_b C_b / E_b$ is a system parameter, with A_b being the cross-sectional area of the SHB bar (126.7 mm^2), C_b the speed of sound of the SHB bar (5790 m/s), and E_b the Young's modulus of the SHB bars (196.5 GPa). The value of $\kappa = 3.7 \times 10^{-12} \text{ m}^5 \text{ N}^{-1} \text{ s}^{-1}$; this value does not affect the calculation of η .

Assume that the deformation of silica foam sample is the only energy dissipation mechanism during a dynamic shear test. A larger value of η indicates a more efficient energy absorption performance. As shown in Fig. 6.6 (b), with the decrease of pore size, more energy is absorbed; the maximum energy absorption efficiency is reached at $\sim 120 \text{ nm}$.

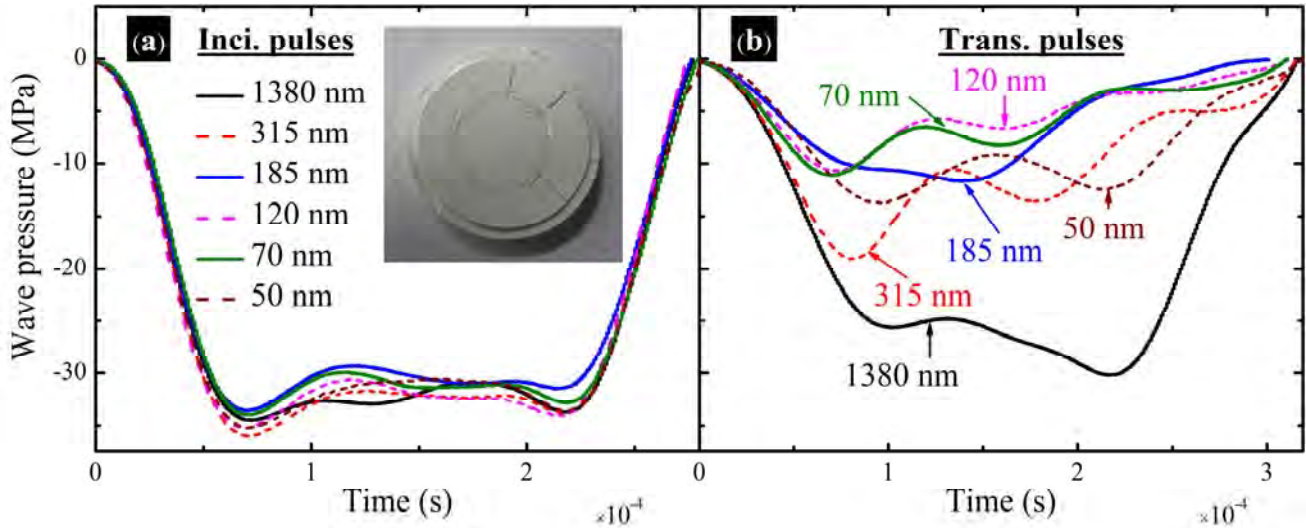


Fig. 6.3 SHB shearing testing curves of PPC-treated silica foams

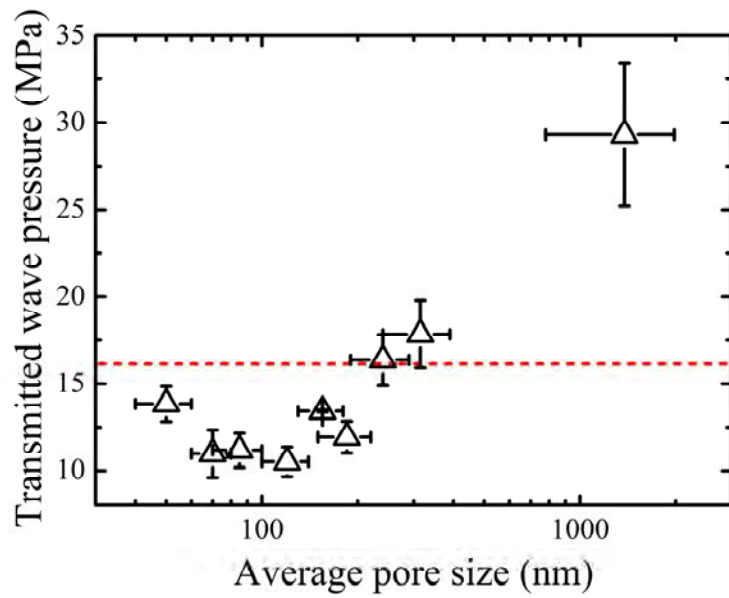


Fig. 6.4 Maximum transmitted wave pressure of PPC-treated silica foams in dynamic shear test. The red dash line indicates the theoretical quasi-static value of 16.1 MPa.

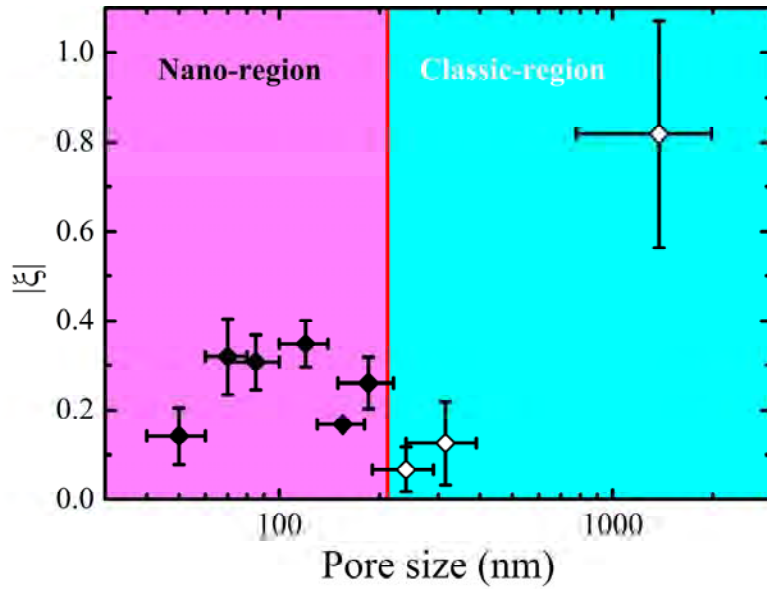


Fig. 6.5 Relative variation of the maximum transmitted wave pressure under the shear strain rate of $\sim 4500 \text{ s}^{-1}$. The entire pore size range under investigation is divided into two regions: Nano-region (solid diamonds with magenta background) and Regular-region (open diamonds with cyan background).

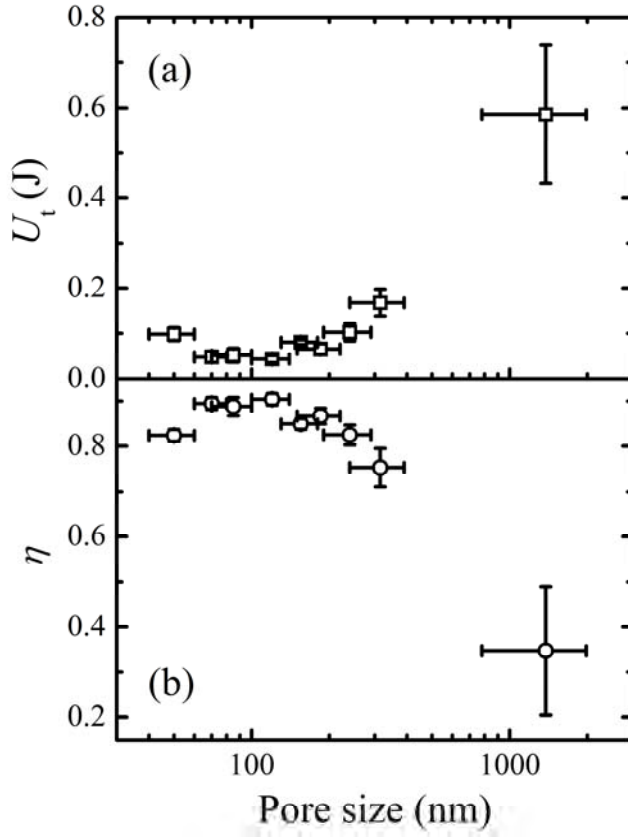


Fig. 6.6 Energy absorption of PPC-treated silica foams under the shear strain rate of $\sim 4500 \text{ s}^{-1}$: (a) transmitted wave energy; (b) effective relative energy absorption.

Table 6.2 Summary of single-parameter testing

	1380±600	315±75	240±50	185±35	155±25	120±20	85±15	70±10	50±10
d (nm)	1380±600	315±75	240±50	185±35	155±25	120±20	85±15	70±10	50±10
D_0 (mm)	22.9±0.9	22.6±0.1	22.3±0.3	22.6±0.4	22.6±0.2	23.5±0.3	23.0±0.3	23.7±0.5	24.2±0.3
h (mm)	4.51±0.02	4.51±0.01	4.53±0.01	4.51±0.01	4.53±0.01	4.53±0.01	4.51±0.01	4.52±0.01	4.52±0.01
p (%)	59.6±2.7	62.7±0.9	61.6±0.9	60.7±1.2	59.5±0.8	62.4±1.4	59.1±2.0	60.0±1.5	60.0±1.3
P_i (MPa)	32.7±0.6	32.3±0.6	31.4±1.2	31.1±0.4	31.3±0.6	32.7±0.6	29.1±0.3	31.3±0.5	31.6±0.2
$P_{t,0}$ (MPa)	15.6	18.3	16.8	15.1	14.1	15.5	12.9	21.0	17.3
$P_{t,c}$ (MPa)	29.9	30.0	30.1	29.6	30.6	28.6	29.4	28.3	28.5
$P_{t,s}$ (MPa)	29.3±4.1	17.8±1.9	16.4±1.5	11.9±0.9	13.4±0.1	10.5±0.8	11.2±1.0	11.0±1.4	13.8±1.0
η	0.35±0.14	0.75±0.04	0.82±0.02	0.87±0.02	0.85±0.01	0.90±0.01	0.89±0.02	0.89±0.01	0.82±0.01

6.5 Deformation Zone

The profile of the deformation zone is measured by using the SEM image analysis technique based on Matlab and Image-Pro Plus.

The criterion of normalized apparent porosity is set to 1.021. As shown in Fig. 6.7, the scanning points with the local normalized porosity higher than this value are marked as black squares. The

red squares outline the boundary of the deformation zone. When the pore size is relatively large, the deformation is concentrated in a narrow band; as the pore size is decreased, the deformation zone becomes increasingly broader.

The area of the deformation zone determines the amount of energy absorbed during the dynamic shearing test. Fig. 6.7 directly shows that shear banding can be efficiently suppressed with the reduction of the pore size, thus promoting widespread energy absorption.

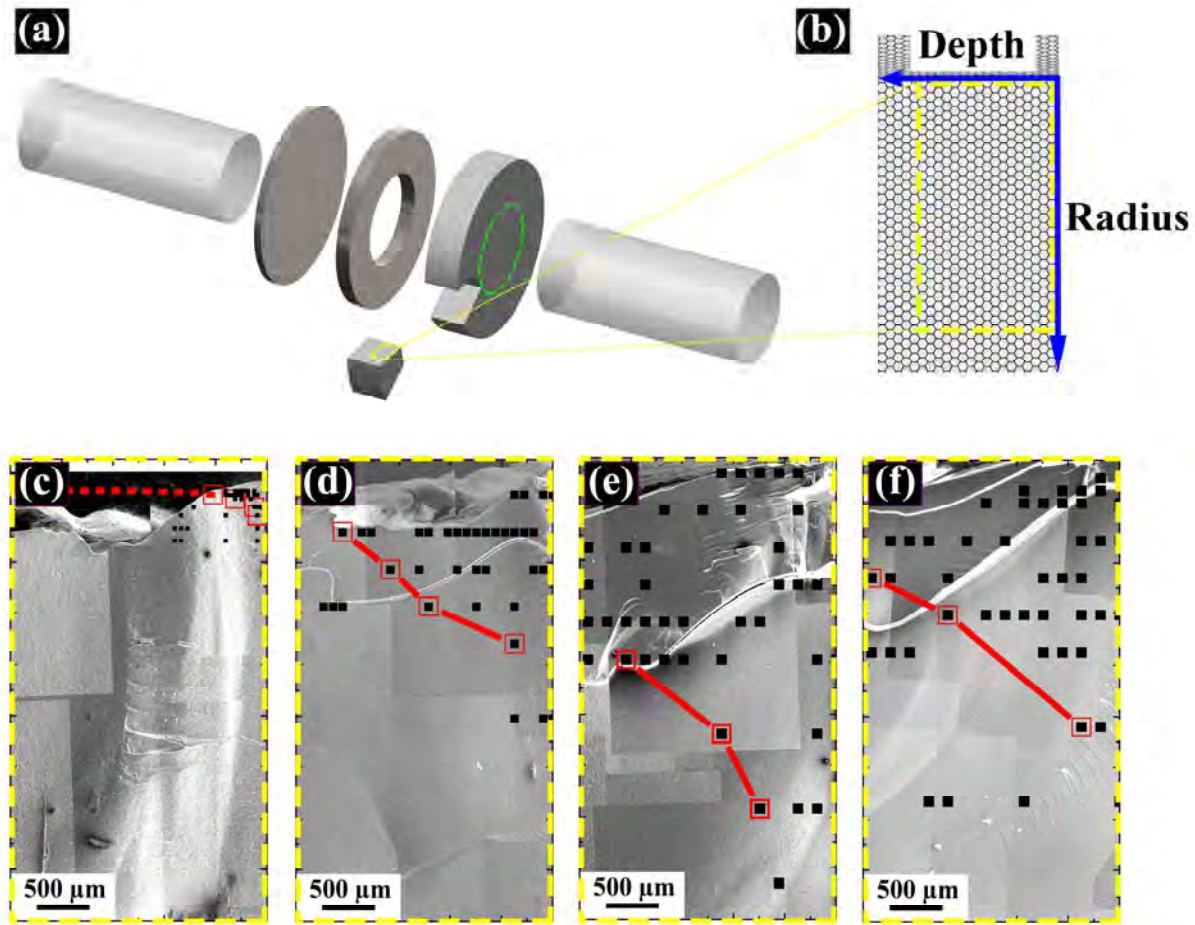
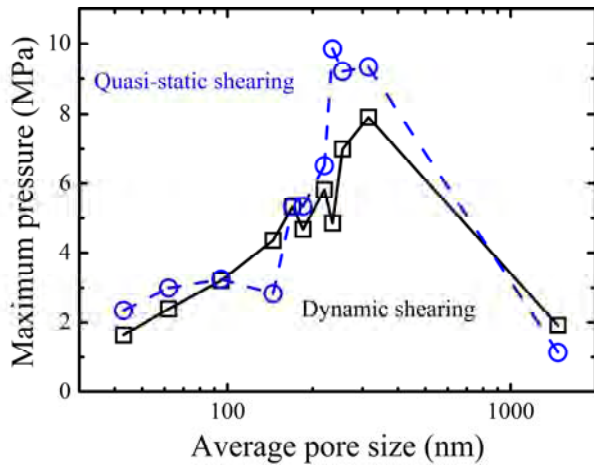


Fig. 6.7 Deformation zones of PPC-treated silica foams at the shear strain rate of 4500 s^{-1} : (a) Extraction of SEM specimens; (b) The Radius-Depth coordinate system; Deformation zones of silica foams with the average pore sizes of (c) 315 nm, (d) 155 nm, (e) 120 nm and (f) 85 nm, respectively. The red lines sketch the boundaries of deformation zones.

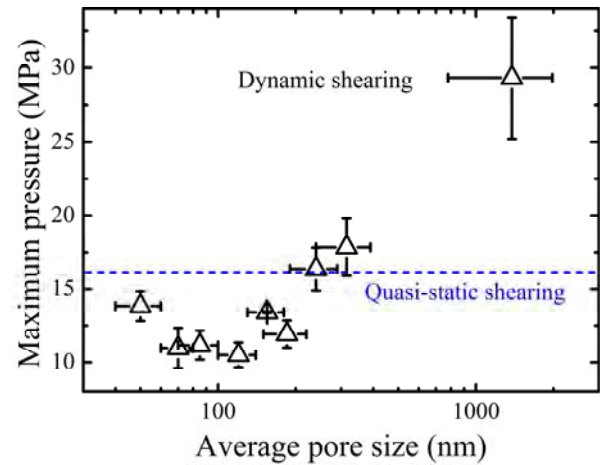
7. ANALYSIS OF EFFECTS OF SHEAR STRAIN RATE

7.1 Pore Size Effect

The two-parameter and the single-parameter testing results are both presented in Fig. 7.1. Other than the variation in the quasi-static shear strength (i.e. the equivalent maximum normal stress) caused by the change in porosity, both results show that the transmitted wave pressure under dynamic shearing can be greatly reduced as the pore size decreases.



(a) Two-parameter testing



(a) Single-parameter testing

Fig. 7.1 Pore size effect in silica foams

The transmitted wave pressure reflects the energy absorption associated with the irreversible deformation of the foam sample, as the porosity, and hence, the impedance, and the impact loading are kept similar in all the tests. That is, the reduction in transmitted wave pressure under dynamic shearing should be related to the energy absorption of the material. For silica foams, the energy absorption is caused by cell buckling.

The extent of the reduction in transmitted wave pressure reflects the amount of the energy being absorbed. Under the same shear strain rate, the more area or volume of the foam involved in cell buckling, the more energy will be dissipated, and thus the lower the transmitted wave pressure would be. In another word, the amount of the energy absorption is a function of the pore size. This has been validated by the SEM image analysis results. For the single-parameter testing, the maximum energy absorption is achieved at the pore size ~ 120 nm.

Under quasi-static shearing, the shear strengths of all the PPC-treated silica foams are similar; while under dynamic shearing, the transmitted wave pressure depends greatly on the pore size. Therefore, the shear strain rate must be an important factor.

Effective shear strain rate equals to the difference between the particle velocities at both ends of the specimen (determined by the impact speed of the titanium tube striker) divided by the shear

gap width (determined by the difference between the radius of the incident bar and the inner radius of the support ring). The two parameters will be discussed later.

Unlike dynamic shearing, the transmitted wave pressure under dynamic compression of all the PPC-treated silica foams shows no sign of pore size effect. Under the one-dimensional loading condition, the cell deformation is always quite uniform throughout the entire sample, no matter what the pore size is. Since no shear localization would happen, changing the pore size does not vary the effective volume of the deformation zone, and thus, the energy absorption capacity is only dependent on the effective compressive strength of the material. The compressive strength is mainly dependent on the porosity, which is similar in all one-parameter samples.

Under quasi-static shearing, shear deformation is always concentrated in the narrow bands between the outer surface of the punch rod and the inner surface of the support ring. Thus, the volumes of deformation zones in all the samples are similar. The quasi-static strength is mainly determined by the porosity, not related to the pore size.

In fact, in SHB tests, as will be shown later, if the striker impact rate was very low, e.g. 5 m/s, the transmitted wave pressure showed no sign of pore size effect. That is, the pore size effect in silica foams must be attributed to the complex interaction between the stress wave and the microstructure of the foam. As a shorter response time of a smaller-pore-sized foam helps promote local hardening, the stress wave front tends to spread to a wider field.

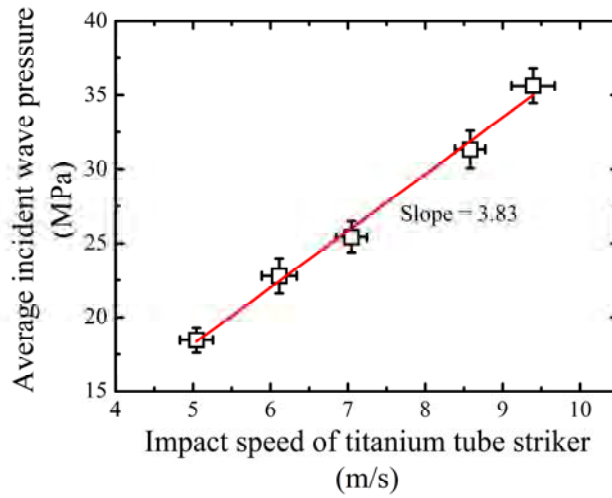


Fig. 7.2 Relationship between the impact speed of titanium tube striker and the average incident wave pressure.

7.2 Effects of Impact Rate

Fig. 7.2 shows the relationship between the striker impact speed and the incident wave pressure. They are linear to each other, suggesting that the SHB system works well in the elastic domain. The slope of the regressed line is $3.83 \text{ MPa}\cdot\text{m}^{-1}\cdot\text{s}$. In the current investigation, all the PPC-treated silica foams have a similar porosity, ~60%, and the shear gap width is set to be 0.20 mm. Based on the single-parameter testing results, we focus on the foams with the pore sizes ranging from tens of nm to hundreds of nm.

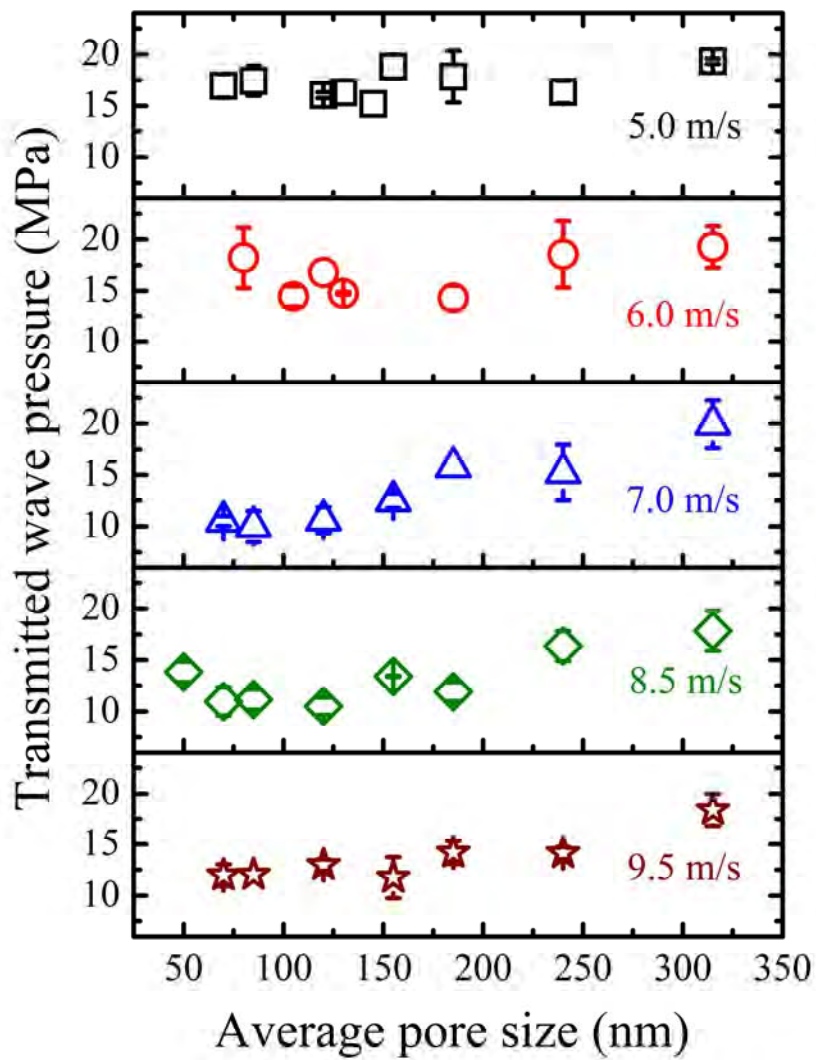


Fig. 7.3 Transmitted wave pressure of PPC-treated silica foams under different impact speeds of the titanium tube striker.

7.2.1 Transmitted Wave Pressure

Fig. 7.3 shows the transmitted wave pressure data as the impact rate changes from 5 m/s to 9.5 m/s. When the impact rate is relatively low, the pore size effect is quite weak, similar to the quasi-static shearing testing result. As the impact rate reaches 6-8.5 m/s, evident pore size effect could be observed; that is, as the pore size is reduced from above ~300 nm to below ~100 nm, the transmitted wave pressure significantly decreases, suggesting that a wider-spread energy absorption is achieved and shear localization is suppressed. When the impact rate is 9.5 m/s, the incident loading is too intense and the samples are completely crashed; the measured data are no longer relevant for energy analysis.

As mentioned previously, the relative variation of the maximum transmitted wave pressure is defined as $|\xi| = |P_{t,s} - P_{t,0}|/P_{t,0}$, where the reference $P_{t,0}$ is 16.1 MPa. When $\xi < 0$ (ξ^-), the transmitted wave pressure is lower than 16.1 MPa, indicating that energy absorption is promoted. As shown in Fig. 7.4, with the increase in the impact speed from 5 m/s, the pressure reduction increases, until the impact rate reaches 8.5-9.5 m/s when the samples are crashed and the wave signal measurement is relatively unreliable. That is, as the impact rate rises, the pore size effect tends to be more pronounced.

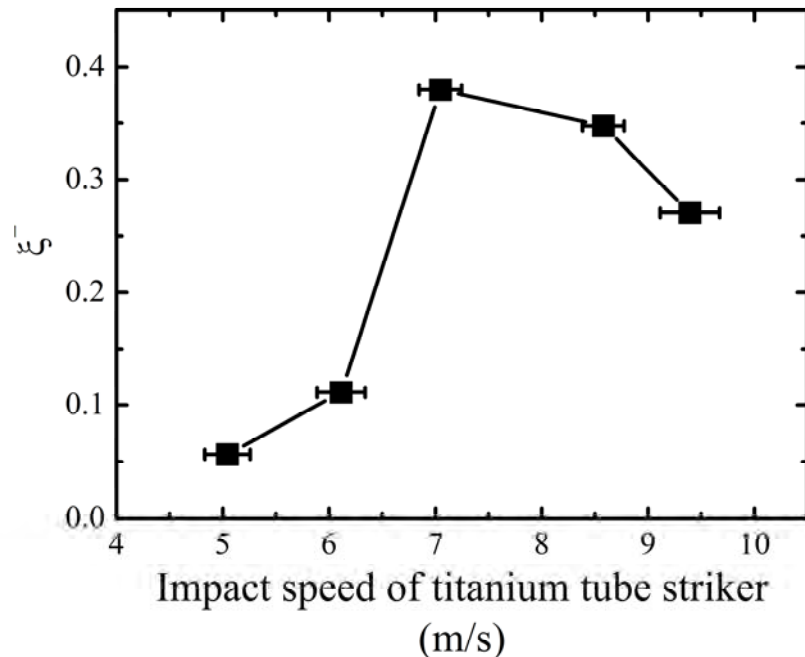


Fig. 7.4 Relative maximum pressure reduction under different impact speeds of the titanium tube striker.

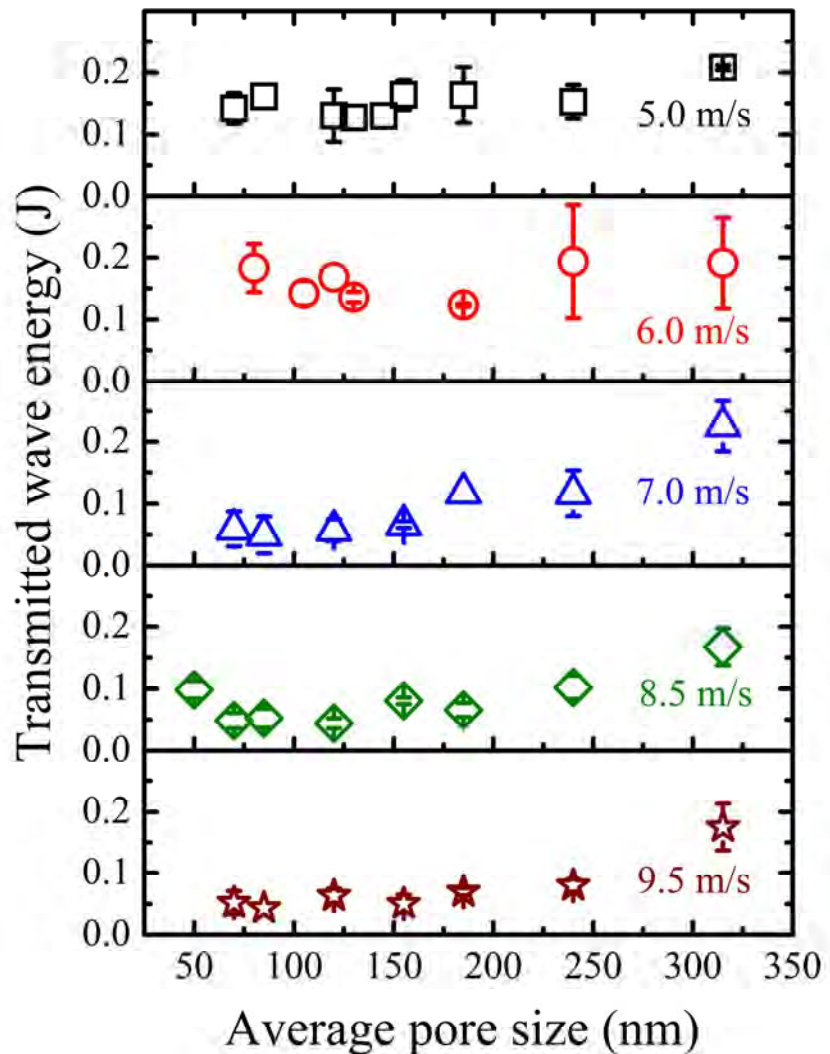


Fig. 7.5 Transmitted wave energy of PPC-treated silica foams under different impact speeds of the titanium tube striker.

7.2.2 Transmitted Wave Energy

In Fig. 7.5, with the increase in impact speed, the transmitted wave energy also shows a size effect. The minimum transmitted wave energy, as shown in Fig. 7.6, continues to decrease with the increase of the impact speed, eventually reaches a plateau. It confirms that as the impact rate rises, the pore size effect on energy absorption is promoted.

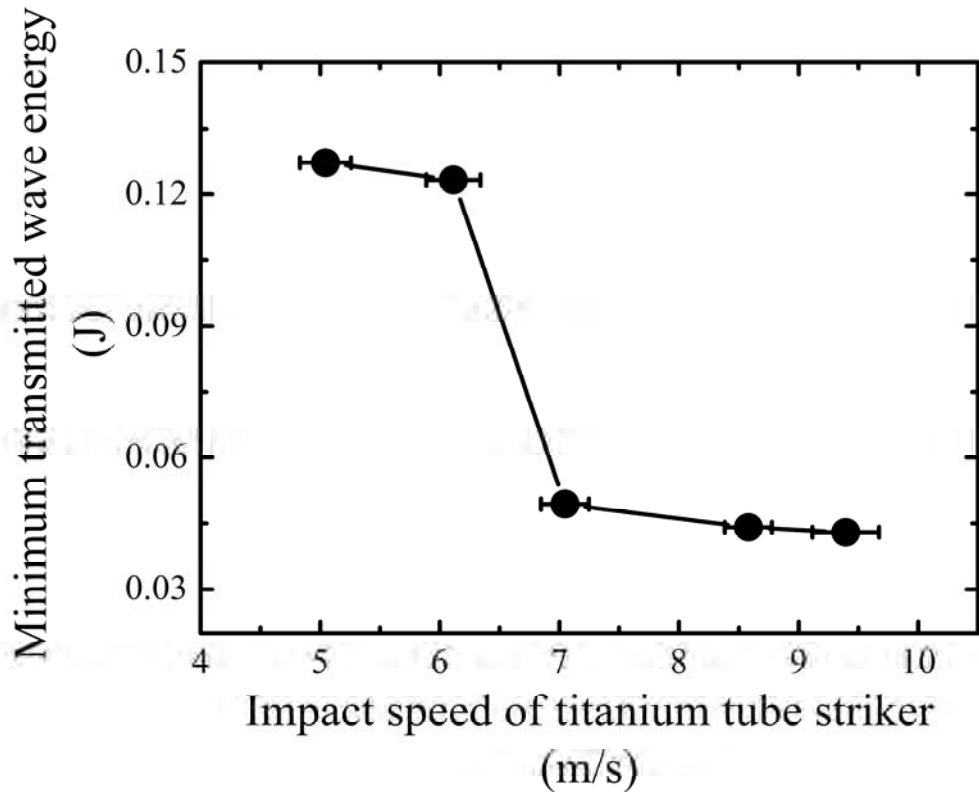


Fig. 7.6 Minimum transmitted wave energy of PPC-treated silica foams under different impact speeds of the titanium tube striker.

7.2.3 Energy Absorption

Assume that, in the SHB test, the sample deformation is the only energy absorption mechanism. The higher the energy absorption efficiency (η), the more energy will be absorbed during the dynamic shearing process. As shown in Fig. 7.7, with the impact speed increasing from 5.0 m/s to 9.5 m/s, the energy absorption efficiency shows a strong impact rate effect. In Fig. 7.8, the maximum energy absorption efficiency continues to increase with the impact speed, and eventually reaches a steady state. In the current investigation, the maximum energy absorption efficiency reaches ~ 0.91 under the striker impact speed of 9.5 m/s.

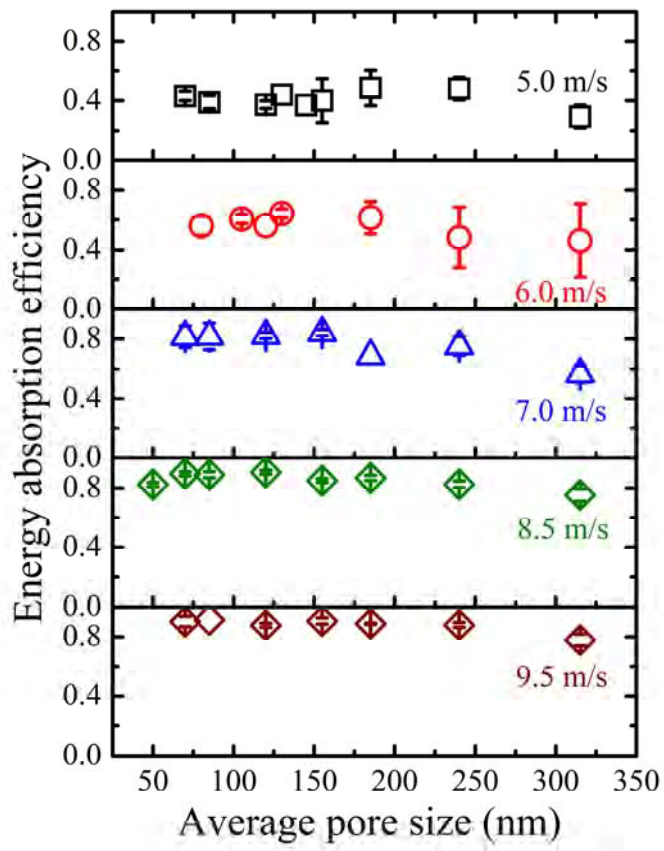


Fig. 7.7 Energy absorption efficiency of PPC-treated silica foams.

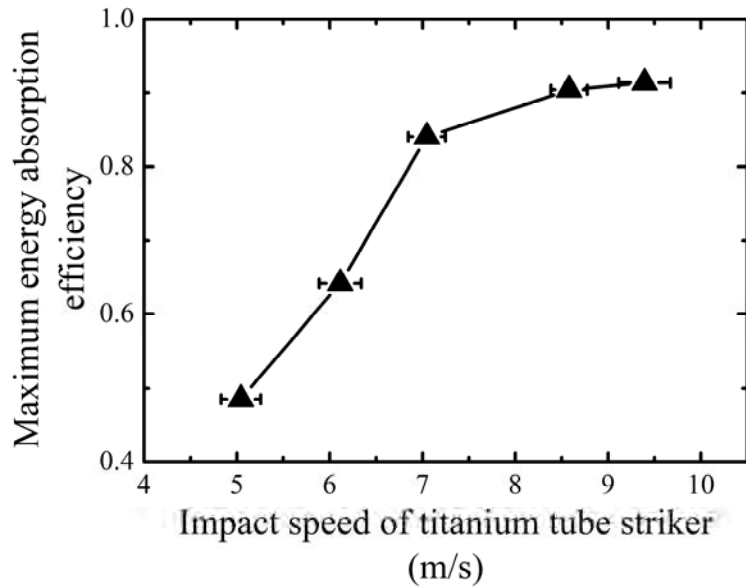


Fig. 7.8 Maximum energy absorption efficiency of PPC-treated silica foams.

7.3 Effects of Shear Gap Width

In the current investigation, another parameter that affects the shear strain rate is the shear gap width of the shear promotion holder (half of the difference between the diameter of the incident bar and the inner diameter of the support ring). We carried out a number of SHB tests on silica nanofoam samples under similar impact loading, with the gap width being varied from 0.40 mm to 0.10 mm. The PPC-treated silica foams had a similar porosity, ~60%. The impact speed of the titanium tube striker is set to be 9.5 ± 0.5 m/s.

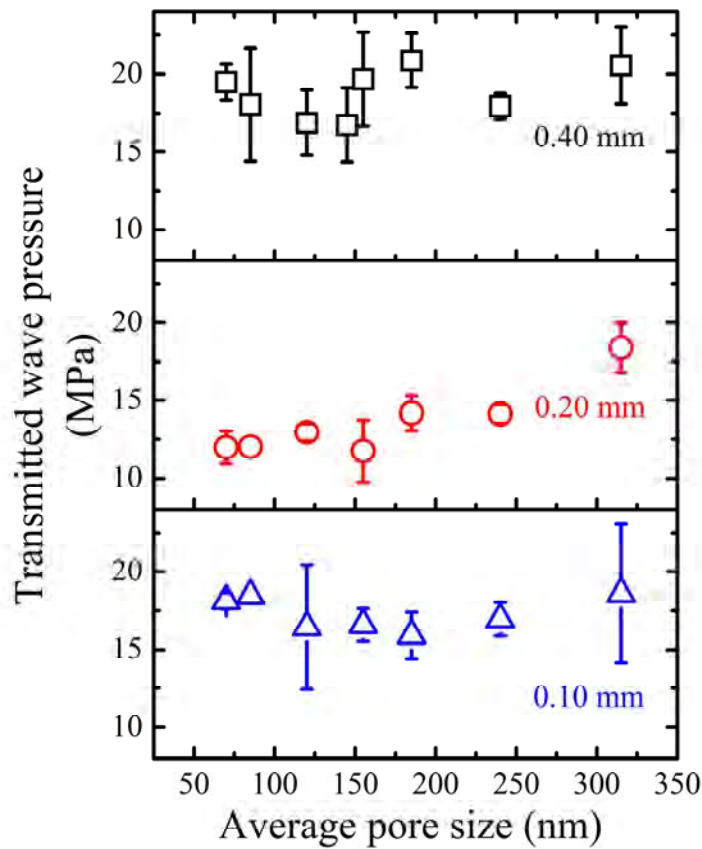


Fig. 7.9 Transmitted wave pressure of PPC-treated silica foams with various shear gap widths.

7.3.1 Transmitted Wave Pressure

In Fig. 7.9, when the gap width is relatively large, there is no evident pore size effect, which is the consistent with the previous result that under a low impact rate, pore size does not influence the transmitted wave pressure. When the gap width is 0.2 mm, the pore size effect is evident, as discussed previously. When the gap width further decreases to 0.1 mm, the data scatter becomes large, suggesting that sample alignment may be a major issue; thus, the measurement data of the

transmitted wave pressure are non-conclusive. Nevertheless, the testing data for the gap widths of 0.4 mm and 0.2 mm agree with the previous result that the pore size effect is promoted as the shear strain rate rises.

7.3.2 Transmitted Wave Energy

In Fig. 7.10, with the decrease of the shear gap width from 0.4 mm to 0.2 mm, the transmitted wave energy shows the similar tendency that, at a higher shear strain rate, an evident pore size effect can be observed. When the gap width is 0.1 mm, the data scatter is large and all the useful information is buried, probably due to the difficulty in accurate alignment of the incident bar, the testing sample, the support ring, and the transmission bar, with the current experimental setups. Similar trend is also observed for the energy absorption efficiency, as shown in Fig. 7.11.

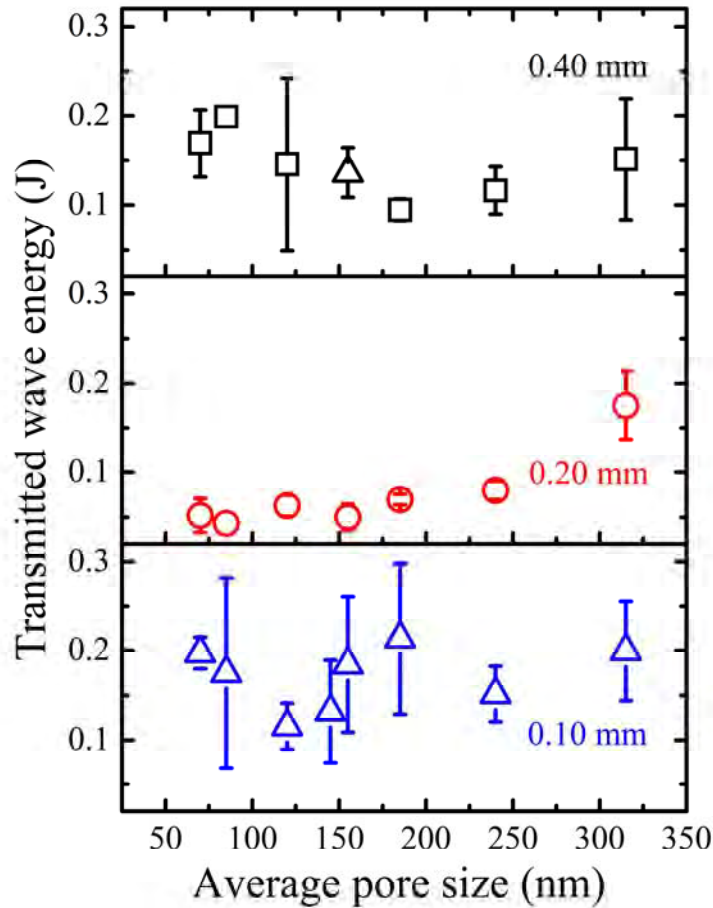


Fig. 7.10 Transmitted wave energy of PPC-treated silica foams with various shear gap widths.

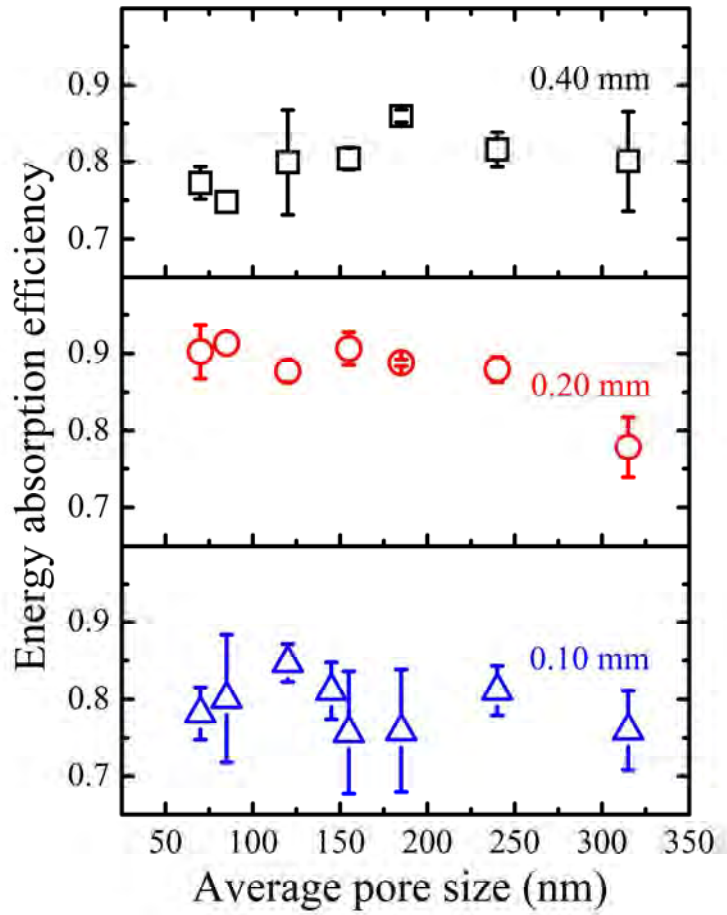


Fig. 7.11 Energy absorption efficiency of PPC-treated silica foams with various shear gap widths.

The testing results of the pore size effect and the shear strain rate effect are listed in Table 7.1. To summarize:

- (1) The pore size effect is evident only when the shear strain rate is sufficiently high.
- (2) For all the shear strain rates under investigation, the transition zone of pore size is around 200-300 nm.
- (3) The current experimental results are non-conclusive for very high strain rates, due to the catastrophic failure of samples under high impact rates or the difficulty in accurate system alignment for small shear gap width.
- (4) The maximum energy absorption efficiency of the PPC-treated silica foams with the porosity ~60% and the thickness of ~4.50 mm, in the current investigation, is ~0.91, with the shear gap width of 0.20 mm and the striker impact speed of 9.5 ± 0.5 m/s; that is, ~90% of wave energy entering into the sample is dissipated.

Table 7.1 Influence of the shear strain rate on the pore size effect

	5.0 ± 0.2	6.1 ± 0.2	7.0 ± 0.2	8.6 ± 0.2	9.4 ± 0.3	9.6 ± 0.2	9.7 ± 0.2
Striker impact speed (m/s)	5.0 ± 0.2	6.1 ± 0.2	7.0 ± 0.2	8.6 ± 0.2	9.4 ± 0.3	9.6 ± 0.2	9.7 ± 0.2
Shear gap width (mm)	0.20	0.20	0.20	0.20	0.20	0.40	0.10
Maximum pressure reduction (MPa)	0.91	1.79	6.11	5.59	4.35	0.19	-0.73
Minimum transmitted wave energy (J)	0.127	0.123	0.049	0.044	0.043	0.095	0.115
Maximum energy absorption efficiency	0.49	0.64	0.84	0.90	0.91	0.86	0.85

8. DYNAMIC INDENTATION TESTS

8.1 Single-parameter Silica Foams

The materials under investigation were a set of silica nanofoams with a similar porosity around 60% and the pore size ranging from tens of nm to hundreds of nm. Details of the materials processing and characterizing have been documented in Section 2. X-ray diffraction (XRD) analysis confirmed that the network materials in all the nanofoam samples were amorphous. Scanning electron microscope (SEM) images proved that all the pores are interconnected and open. Fig. 8.1 (c) shows a foam sample. The material parameters are listed in Table 8.1.

Solid silica monoliths were obtained by using a similar approach as the silica nanofoams, but were fired to the full density (2.2 g/cm^3) at a temperature slightly higher than T_s for 12 hours (see Section 2). Similar as silica foams, the solid silica samples were polished, and their final thickness was $4.54 \pm 0.01 \text{ mm}$.

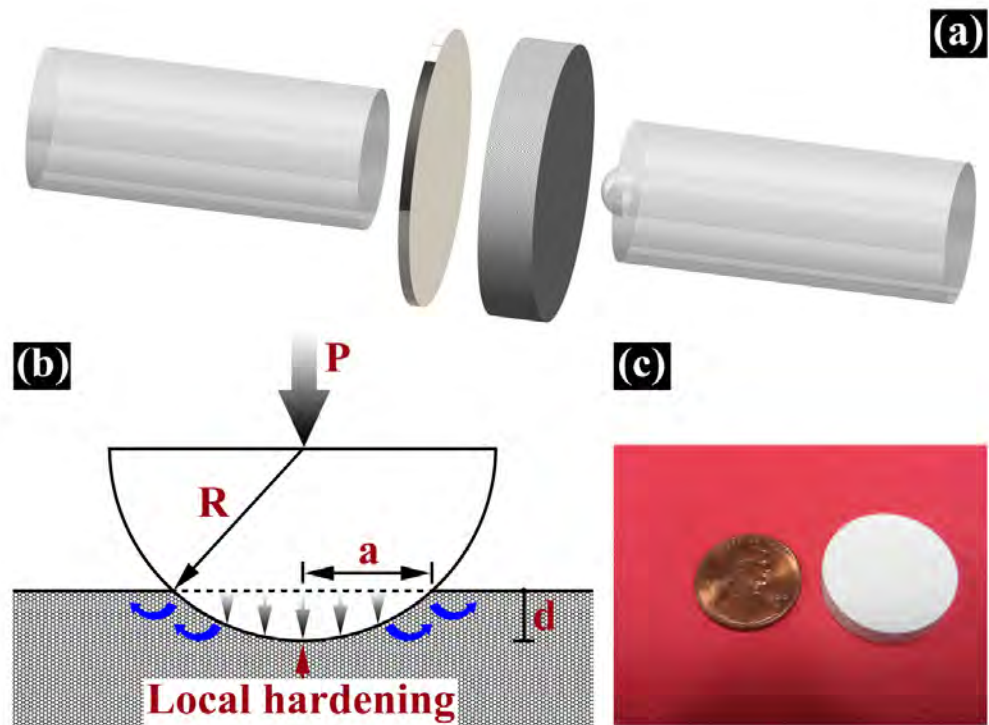


Fig. 8.1 (a) Schematic of the dynamic indentation setup. (b) Mechanism of local hardening in a silica nanofoam. (c) Photo of a silica nanofoam sample.

Table 8.1 Material parameters and indentation results

Pore size (nm)	700±440	275±90	210±60	165±45	145±30	105±15	80±15	50±10	Solid silica
Porosity (%)	59.7±1.0	60.7±1.2	59.9±0.6	59.8±1.2	60.6±1.1	61.4±1.4	60.5±0.5	60.5±0.5	<1%
Thickness (mm)	4.52±0.01	4.54±0.01	4.53±0.01	4.54±0.01	4.53±0.01	4.54±0.01	4.53±0.01	4.54±0.01	4.54±0.01
Quasi-static indentation	Maximum Force (N)	300	300	300	300	300	300	300	300
	Indentation Size (μm)	676±4	610±8	668±5	662±9	640±22	685±6	670±5	673±7
Dynamic indentation	Maximum Force (N)	687±185	721±19	729±90	670±29	683±39	686±2	759±191	819±114
	Indentation Size (μm)	1353±75	1272±18	1210±98	1292±74	1193±62	1146±19	1045±1	933±13

Note: Maximum force under dynamic indentation equals the peak value of the transmitted wave pressure times the cross section area of the SHB rods.

8.2 Indentation Tests

Dynamic indentation tests were conducted using the same set of Split Hopkinson Bar (SHB) system as dynamic shearing. In the investigation, a hardened steel hemispherical indenter with the diameter of 4.75 mm, the hardness of 91 HRA, and the surface roughness of 0.7 micro inch Ra maximum was employed. As shown in Fig. 8.1 (a), the indenter was firmly attached to the end of the incident bar by VISHAY M-Bond 200 adhesive, and the silica nanofoam sample was sandwiched in between the indenter and a stainless steel substrate. The striker speed was 8.6±0.2 m/s, and the velocity of the incident bar was around 0.9 m/s. Thus, the compressive strain rate of the nanofoam sample (thickness ~4.50 mm) was about 200 sec⁻¹. Fig. 8.2 (a2)-(e2) show typical indented samples. For each type pore size, at least three samples were tested to average. For solid silica samples, tungsten carbide hemispherical indenter of the same size was employed.

Quasi-static indentation tests were conducted on the same set of silica nanofoams using an Instron 5582 machine at the loading/unloading rate of 0.01 mm/min, and the maximum force of 300 N. The indenter and the sample mounting setup were identical to that of the dynamic indentation tests. Fig. 8.2 (a1)-(e1) show typical quasi-statically indented samples. For each pore size, at least three samples were tested.

The solid silica disk samples were also analyzed in quasi-static and dynamic indentation tests. The testing conditions were the same as that of the silica nanofoams. Fig. 8.3 shows typical solid silica samples after indentation tests.

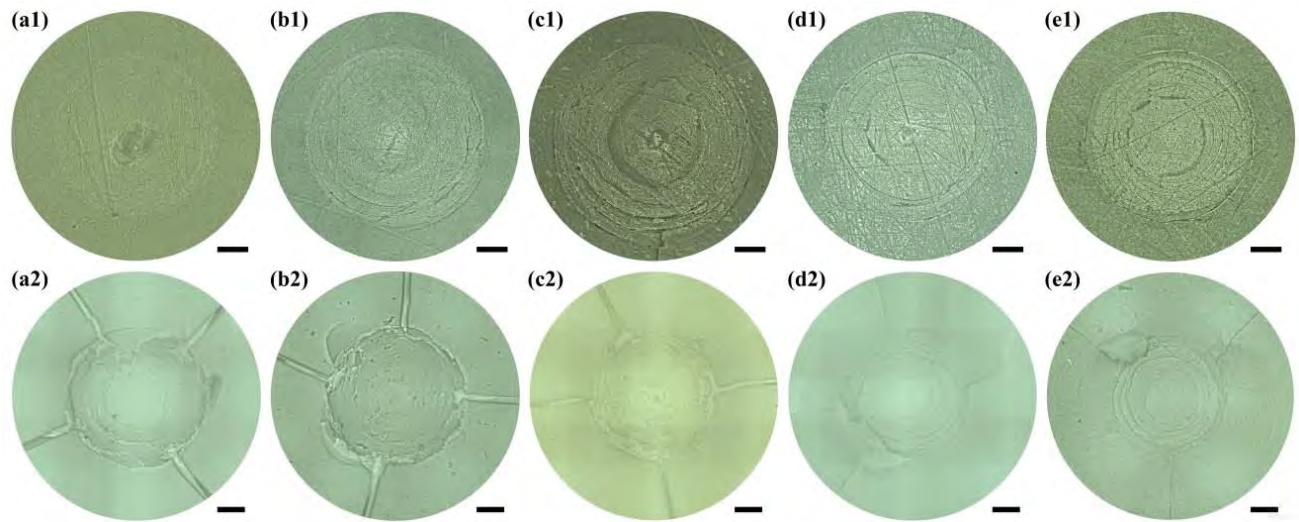


Fig. 8.2 Typical damages of silica nanofoams caused by quasi-static and dynamic indentation tests: (a) 275 nm; (b) 165 nm; (c) 105 nm; (d) 80 nm; (e) 50 nm. (a1)-(e1) are for quasi-static testing with the scale bars of 250 μm ; (a2)-e(2) are for dynamic indentation with the scale bars of 500 μm .

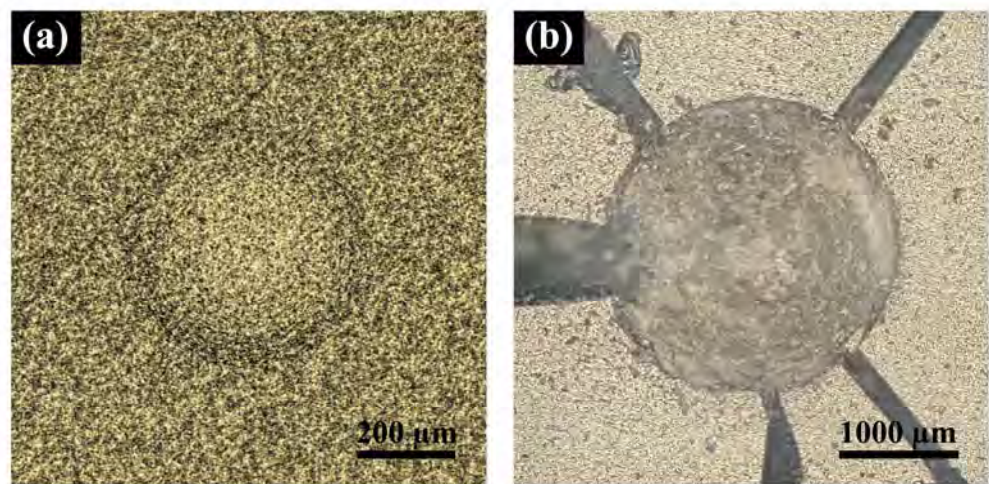


Fig. 8.3 Typical indentations in solid silica caused by (a) quasi-static and (b) dynamic loadings.

8.3 Testing Results

After testing, the indented silica samples were well preserved and a Keyence VHX-1000 digital microscope was employed to measure their indentation sizes and depth profiles. The indentation size was defined as the radius of the indentation. Fig. 8.4 exhibits the indentation size as a function of the pore size under quasi-static and dynamic loadings. Fig. 8.5 (a) and Fig. 8.6 (a) show the typical profiles of quasi-static and dynamic indentations, respectively. With the original surface (far field) as the reference, the lowest point determines the indentation depth. Fig. 8.5 (b) and Fig. 8.6 (b) exhibit the indentation depth as a function of the pore size.

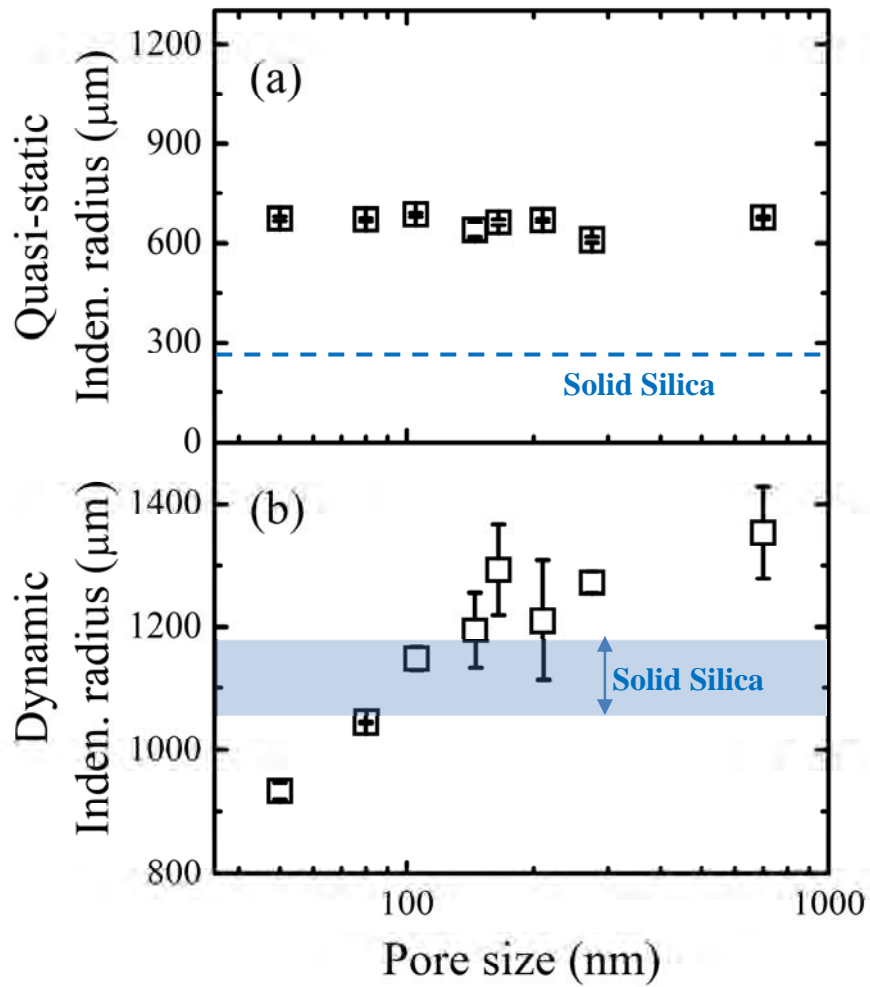


Fig. 8.4 Indentation sizes of (a) quasi-static and (b) dynamic tests.

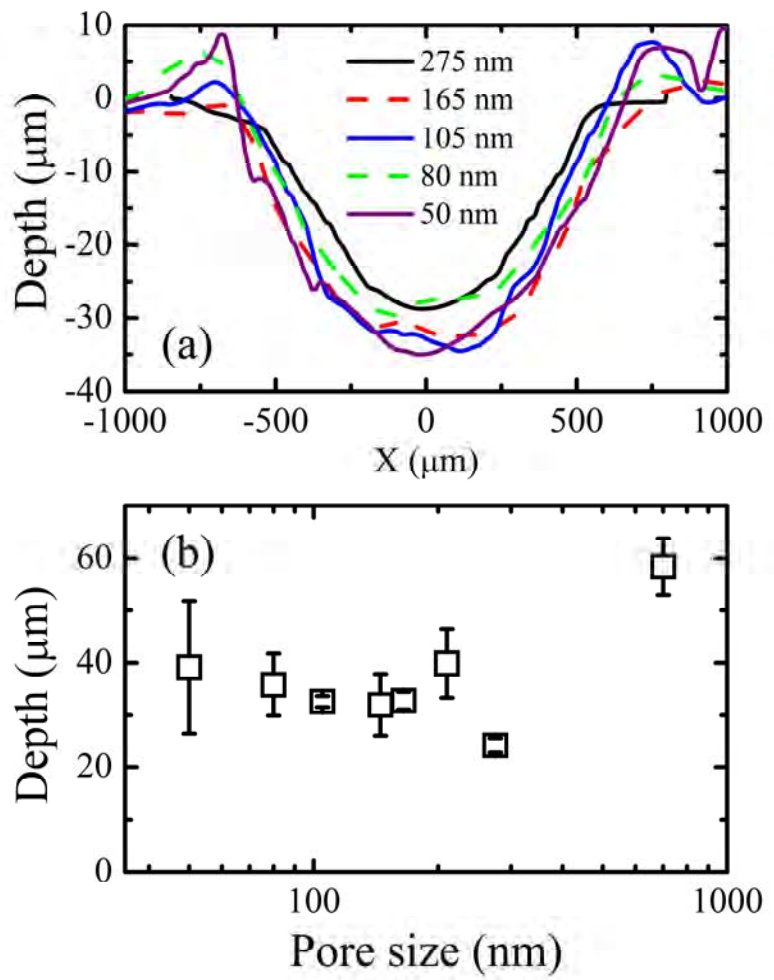


Fig. 8.5 Quasi-static indentation results of silica nanofoams: (a) typical cross-section profiles of indentations; and (b) indentation depth as a function of pore size.

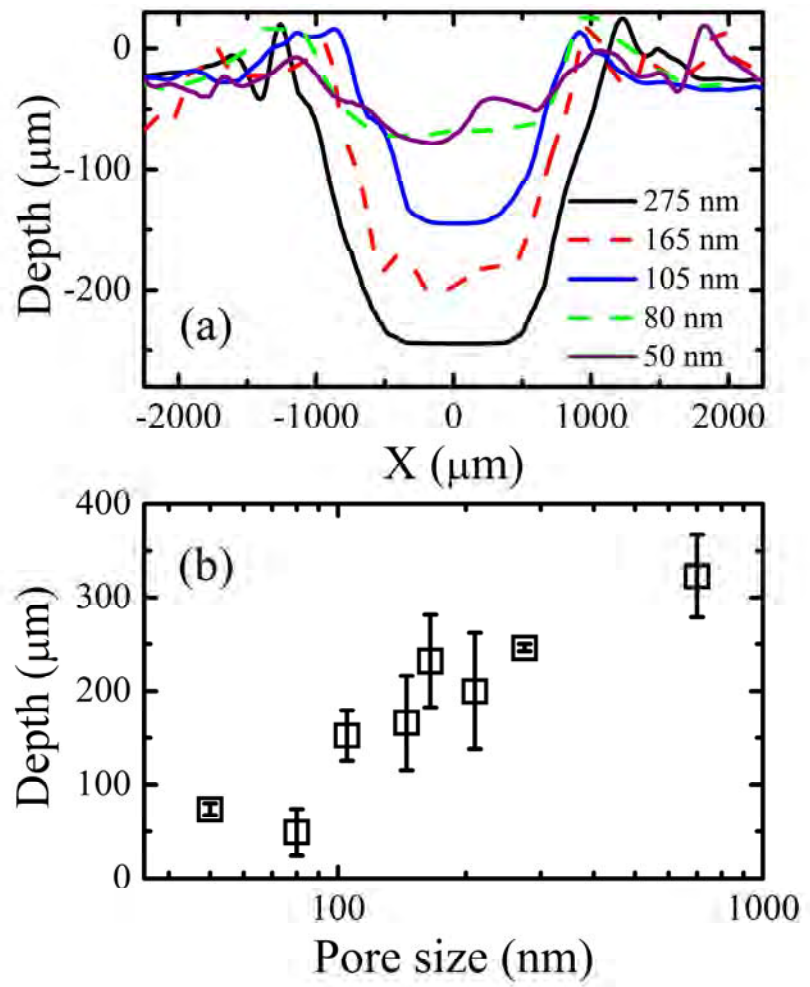


Fig. 8.6 Dynamic indentation results of silica nanofoams: (a) typical cross-sectional profiles of indentations; and (b) indentation depth as a function of the pore size.

9. CONCLUSIONS AND FUTURE WORK

In this project, we systematically investigated dynamic behaviors of silica nanofoams with the porosity of ~60% and the pore size ranging from tens of nm to more than 1 μm . The following conclusions are drawn:

- 1) When the pore size is below 200 nm, the nanofoam offers a much higher resistance to indenter penetration under dynamic loadings, compared with larger-pore-sized foams and even solid silica samples (**Section 8**). This finding may open a door to the development of lightweight, high-performance armor plates.
- 2) When the pore size is below 200 nm, under dynamic shear loadings shear localization is suppressed and widespread energy absorption is promoted; as a result, the transmitted wave pressure is much lower than that of larger-pore-sized silica foams (**Section 6**). This finding may open a door to the development of lightweight, high-performance armor cushioning layers.
- 3) The behaviors of nanofoams under quasi-static shear, quasi-static indentation, and dynamic compression loadings are similar with that of larger-pore-sized silica foams, suggesting that the above beneficial properties of nanofoams are associated with highly nonlinear, highly heterogeneous dynamic loadings.

If the result of silica nanofoams can be repeated on nanofoams of hard materials, e.g silicon carbide and high strength alloys that are currently being used in armor plates, under high-speed bullet impact conditions, it would provide a promising approach to largely reduce weight/thickness of an armor and simultaneously, improve its protection effectiveness.

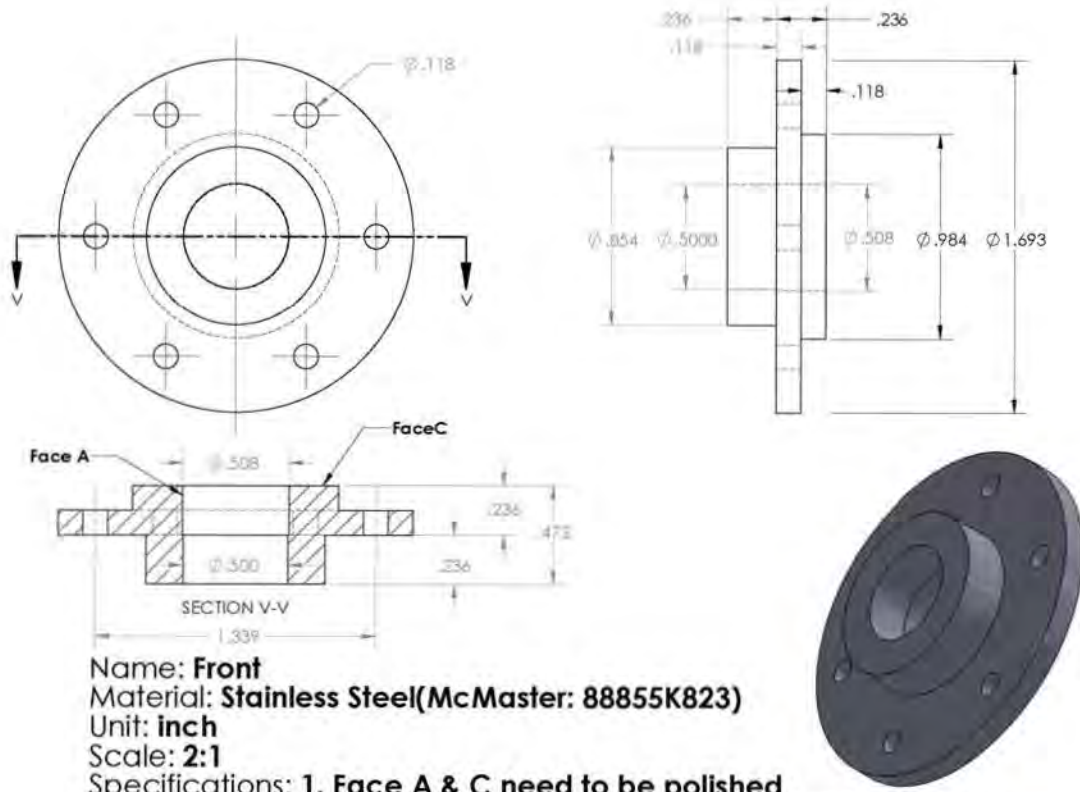
If the result of silica nanofoams can be repeated on nanofoams of soft materials such as polypropylene and polyurathene, it would provide a promising approach to develop high-performance cushioning layers, for mitigation of blast lung problems and traumatic brain insuray (TBI).

These will be the focus of our future work.

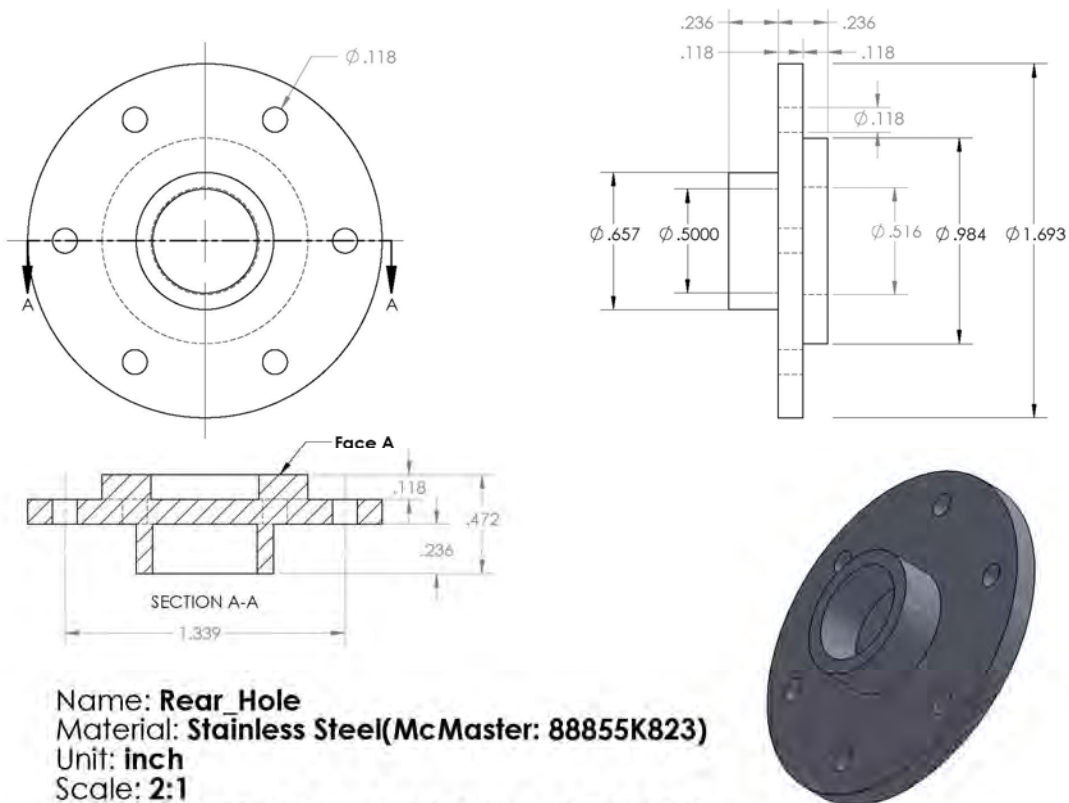
APPENDIX

A. Mechanical Drawings of Shear Promotion Holder

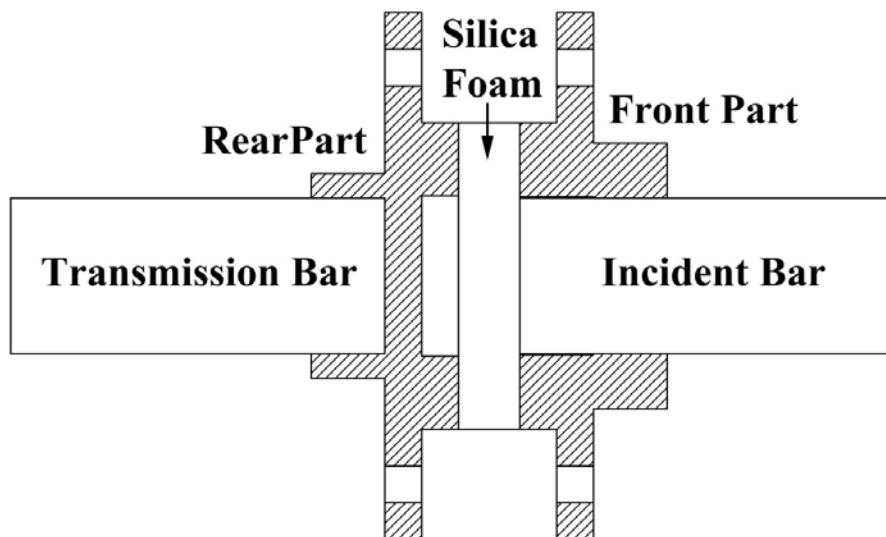
A.1 Front Part



A.2. Rear Part



A.3. Assembly Drawing



B. Codes for SEM Image Enhancement

```
Option Explicit
Sub BestFitting()

    Dim i As Integer
    Dim j As Integer
    Dim k As Integer
    Dim N As Integer
    Dim Temp_Arr2 As String
    Dim Temp_Path2 As String

    Dim folderGrayImageSFC As String
    Dim OutputFolderGrayImageSFC As String
    Dim fname(35) As String

    For i = 1 To 35
        If i < 10 Then
            fname(i) = "0" & Str(i)
        ElseIf i <= 34 Then
            fname(i) = Str(i)
        Else
            fname(i) = "00"
        End If
    Next i

    For i = 1 To 35
        For j = 1 To 35
            For k = 1 To 10

                folderGrayImageSFC = "C:\Users\zcngu\Desktop\SilicaFoam12102013\CalAP\#06-
11\GrayScaleImages\OriginalImage\SilicaFoam12102013_#06-11-01_R" & fname(i) & "_" & fname(j) & "_" &
fname(k) & ".tif"

                OutputFolderGrayImageSFC = "C:\Users\zcngu\Desktop\SilicaFoam12102013\CalAP\#06-
11\GrayScaleImages\SCFP\StdDev\SilicaFoam12102013_#06-11-01_R" & fname(i) & "_" & fname(j) & "_" &
fname(k) & "_StdDev.tif"

                folderGrayImageSFC = Replace(folderGrayImageSFC, " ", "")
                OutputFolderGrayImageSFC = Replace(OutputFolderGrayImageSFC, " ", "")

                If Dir(folderGrayImageSFC) = "" Then
                Else
                    ret = IpWsLoad(folderGrayImageSFC, "TIF")
                    ret = IpAoiShow(FRAME_NONE)
                    ipRect.Left = 1
                    ipRect.top = 1
                    ipRect.Right = 645
                    ipRect.bottom = 482
                    ret = IpAoiCreateBox(ipRect)
                    ret = IpWsCopy()
                    ret = IpFltLocHistEq(60, 1, 6, 0.5)
                    ret = IpFltMedian(5, 2)
                    ret = IpFltGauss(5, 10, 1)
                    ret = IpFltClose(MORPHO_5x5OCTAGON, 2)
                    ret = IpFltShow(0)
                End If
            Next k
        Next j
    Next i
End Sub
```

```
    ret = IpAoiShow(FRAME_NONE)
    ret = IpWsSaveAs(OutputFolderGrayImageSFC, "tif")
    ret = IpDocClose()

End If

Next k
Next j
Next i

End Sub
```

C. Dynamic indentation

Our experimental setup was similar with the dynamic hardness measurement system developed by Koeppel and Subhash [21-23]. They investigated dynamic hardness of a variety of materials using a Vickers indenter. Fig. C.1 shows their experimental setup. Fig. C.2 shows the quasi-static and dynamic results. Fig. C.3 exhibits the relationship between the yield strength and the hardness. In their study, the dynamic (DHV) and quasi-static hardness (HV) were calculated from the same equation, $DHV=HV=P/A=1.8544\cdot P/d^2$, where P is the indentation load and d is the mean diagonal of the indentation. In our study, spherical indenter was employed; thus, $A=\pi a^2$, where $a=(R\cdot d)^{1/2}$ is the contact radius and R and d are the radii of the indenter and the indentation, respectively

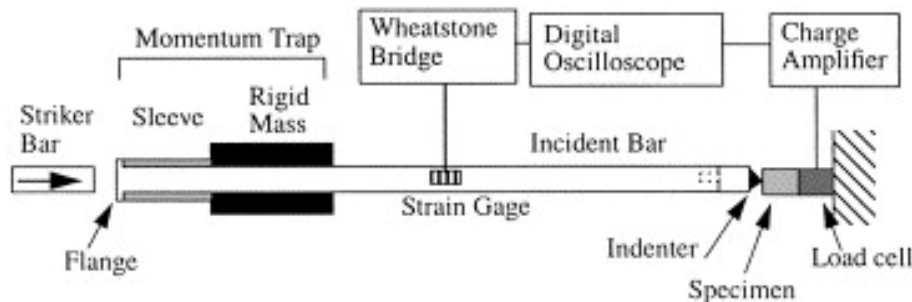


Fig.C.1 Dynamic indentation setup [26]

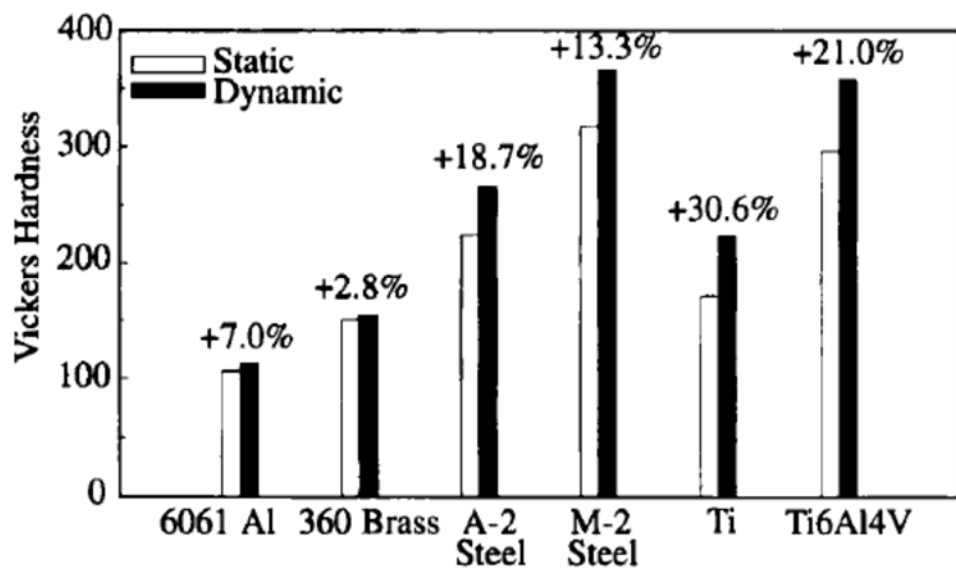
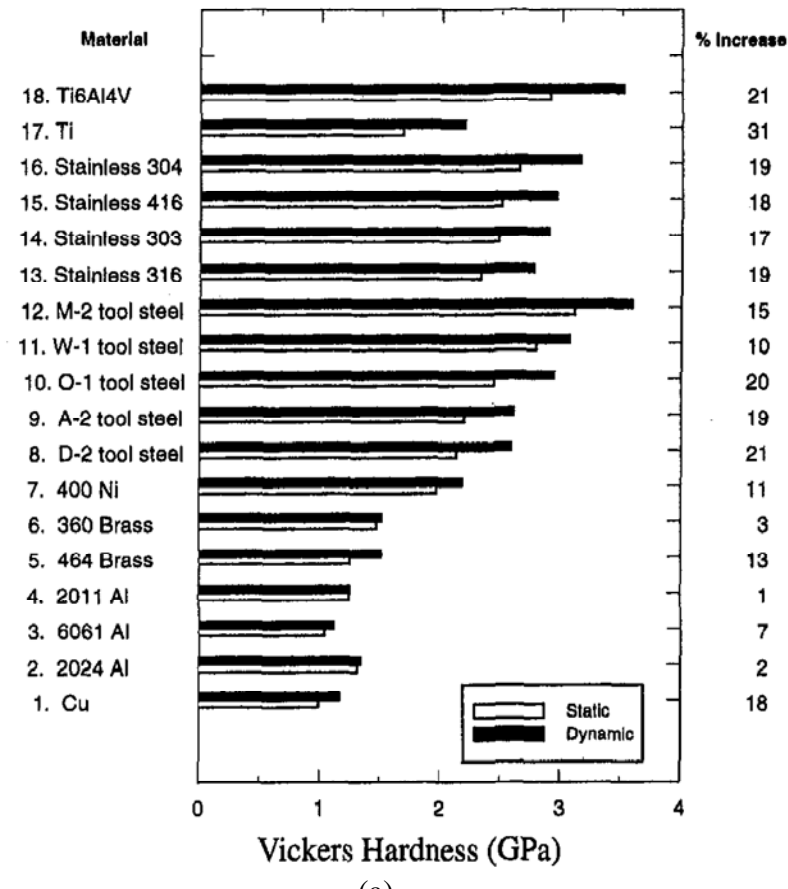
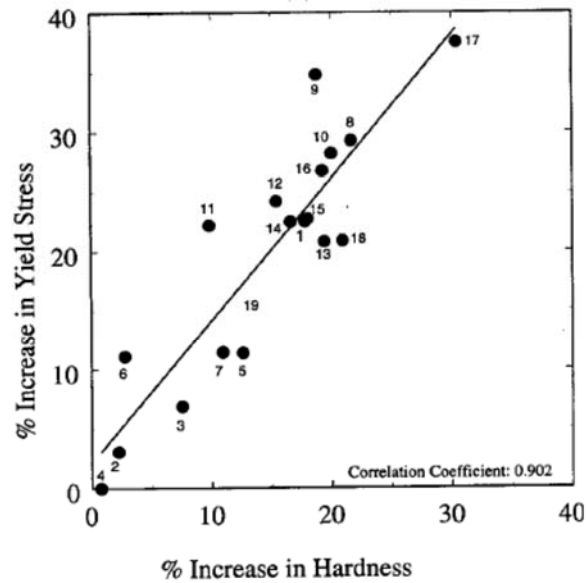


Fig.C.2 Static and dynamic Vickers hardness of metals [27].



(a)



Correlation Coefficient: 0.902

(b)

Fig.C.3 Relationship between the yield stress and the hardness [28].

REFERENCES

- [1] R. D. Shoup, in *Colloid and Interface Science*, edited by M. Kerker (Academic Press, New York, 1976), pp. 63.
- [2] R. Miyamoto, Y. Ando, C. Kurusu, H. z. Bai, K. Nakanishi, and M. Ippommatsu, Journal of separation science **36**, 1890 (2013).
- [3] K. Nakanishi, Journal of Porous Materials **4**, 67 (1997).
- [4] K. Nakanishi, in *Monolithic Silicas in Separation Science: Concepts, Syntheses, Characterization, Modeling and Applications* (John Wiley & Sons, 2010), p. 11.
- [5] J. Mackenzie, Journal of the American Ceramic Society **47**, 76 (1964).
- [6] C. J. Brinker and G. W. Scherer, *Sol-gel science: the physics and chemistry of sol-gel processing* (Gulf Professional Publishing, 1990).
- [7] R. K. Iler, *The chemistry of silica: solubility, polymerization, colloid and surface properties, and biochemistry* (Wiley, 1979), p.^pp. 645.
- [8] T. Kawaguchi, J. Iura, N. Taneda, H. Hishikura, and Y. Kokubu, Journal of Non-Crystalline Solids **82**, 50 (1986).
- [9] Y. Diao, T. Harada, A. S. Myerson, T. Alan Hatton, and B. L. Trout, Nat Mater **10**, 867 (2011).
- [10] L. J. Gibson and M. F. Ashby, *Cellular solids: structure and properties* (Cambridge university press, 1999).
- [11] E. W. Washburn, Physical Review **17**, 273 (1921).
- [12] R. Pirard, C. Alie, and J.-P. Pirard, Handbook of Sol-Gel Science and Technology. Volume II: Characterization of Sol-Gel materials and Products, 211 (2005).
- [13] S. Nemat-Nasser, J. B. Isaacs, and J. E. Starrett, Proceedings of the Royal Society of London. Series A: Mathematical and Physical Sciences **435**, 371 (1991).
- [14] B. Song and W. Chen, Experimental Mechanics **44**, 622 (2004).
- [15] V. F. Nesterenko, *Dynamics of heterogeneous materials* (Springer, 2001).
- [16] M. A. Meyers, Y. B. Xu, Q. Xue, M. T. Pérez-Prado, and T. R. McNelley, Acta Materialia **51**, 1307 (2003).
- [17] M. A. Meyers, L. E. Murr, and K. P. Staudhammer, *Shock-wave and high-strain-rate phenomena in materials* (CRC, 1992).
- [18] C. C. Reyes-Aldasoro, Electronics letters **45**, 454 (2009).
- [19] N. Otsu, Automatica **11**, 23 (1975).
- [20] F. B. Surani, X. Kong, D. B. Panchal, and Y. Qiao, Applied Physics Letters **87**, 163111 (2005).
- [21] R. J. Anton and G. Subhash, Wear **239**, 27 (2000).

- [22] G. Subhash, B. Koeppel, and A. Chandra, Journal of engineering materials and technology **121**, 257 (1999).
- [23] B. Koeppel and G. Subhash, Experimental Techniques **21**, 16 (1997).